STRAIN GAUGE UTILIZATION FOR AERIAL VEHICLE DYNAMIC LOAD MEASUREMENT

A Thesis
IN
Mechanical Engineering

Presented to the Faculty of the University
of Missouri–Kansas City in partial fulfillment of
the requirements for the degree

MASTER OF SCIENCE

by
JOHN BAZIN

B. S., University of Missouri - Kansas City 2015

Kansas City, Missouri
2016

STRAIN GAUGE UTILIZATION FOR AERIAL VEHICLE DYNAMIC LOAD MEASUREMENT

John Bazin, Candidate for the Master of Science Degree

University of Missouri–Kansas City, 2016

ABSTRACT

The strain gauge is a commonly used tool for dynamic load and strain measurement of a system. The work presented in this thesis describes the development and evaluation of strain gauges applied to both an aerodynamic decelerator system and an unmanned aerial vehicle. This thesis has three main objectives: (1) develop and evaluate test a circular parachute strain gauge-based load distribution measurement system, (2) develop and evaluate a strain gauge thrust estimation system for a quadrotor unmanned aircraft, and (3) compare the developed strain gauge-based thrust estimation technique with an indirect real time parameter estimation technique for motor fault detection.

In pursuit of the first thesis objective, a load distribution measurement system for the suspension lines of circular parachutes was developed. The motivation to create a load distribution measurement system stems from parachute system design traditionally requiring an extensive flight testing regimen. Numerical solution-based design is difficult

due to the highly nonlinear deformation behavior of the parachute canopy. Traditionally, circular parachutes are assumed to have symmetric canopy loading upon inflation and during terminal descent. Asymmetric canopy loading can have a significant impact on circular parachute suspension line loads, but is typically neglected. The developed strain gauge-based load distribution measurement system for circular parachutes has wireless capabilities and can be readily applied to a wide variety of aerodynamic declarator systems. The developed system can be used to observe asymmetric behaviors in order to help determine the significance of asymmetric canopy loading. Custom strain gauge load cells with mounted custom circuitry to calibrate, amplify, and transmit the load data were fixed to canopy suspension lines. Parachute drop testing was performed to evaluate the effectiveness to identify any significant asymmetric canopy loading behavior. Drop testing was performed with a 1.2m (4.0ft) quarter-spherical cross based canopy with a payload of 2.0kg (4.4lbs). A 12m (39ft) guide-line based drop rig was implemented to prevent canopy rotational movement that could hinder testing repeatability. Load distribution data was first verified via both static calibration and in-flight total canopy load measurements. Drop testing was then conducted to identify loading asymmetry during both inflation and terminal descent. Results demonstrated the use of the strain gauge-based load distribution measurement system for measuring significant asymmetric canopy loading patterns.

In pursuit of the second thesis objective, strain gauges were used to aid in the development of a thrust estimation system for individual motors/propellers of a small

quadrotor unmanned aerial vehicle (UAV). Small UAVs have become increasingly utilized for a wide range of applications; however, such aircraft typically do not undergo the same rigorous safety protocols as their larger human-piloted counterparts. A thrust estimation technique for a quadrotor unmanned aircraft was developed and evaluated that could potentially improve flight control design by increasing sensory feedback information. Strain gauges were integrated into the quadrotor frame to provide total force measurements on each arm of the aircraft. A dynamic model coupled with state information from motion capture and on-board measurement data was implemented to compensate for inertial forces caused by rotational and translational acceleration. Testing was conducted to evaluate the accuracy of the individual load cells, inertial compensation, and free-flight motor thrust estimates. Results demonstrate inertial force compensation during high frequency aircraft motion, which could potentially be useful for detecting an in-flight failure. The measurement system therefore has the potential to quickly detect an in-flight failure.

The focus of the third thesis objective is to expand on the development of the thrust estimation system by performing an evaluation of the fault detection capabilities. A comparative study was conducted of the thrust estimation system along with a real-time parameter estimation in the frequency domain during two motor failure scenarios of a small quadrotor UAV. Detecting and mitigating disturbances caused by in-flight motor/propeller failures is an important aspect of a robust flight controller for multirotor aircraft. The comparative study was performed in an attempt to determine whether direct

thrust estimation (strain gauge-based) or indirect thrust estimation (parameter estimation using on-board measurement) more accurately and quickly capture an in-flight failure. Flight test results were post-processed to mimic real-time parameter estimation and strain gauged-based fault detection. Results show the strain gauge-based parameter estimation exhibits noisy estimates, but does have faster response to the failure. The parameter estimation using onboard data does not respond to failures as quickly as the strain-gauge based technique, but does produce better parameter estimate stability. Although both estimation techniques display strengths and weaknesses, neither technique is optimal for real time failure detection individually. A combination of the real-time parameter estimation in the frequency domain and the strain gauge-based thrust estimation techniques may yield a fast yet stable fault detection system. The evaluation of the fault detection capabilities of the thrust estimation system did not prove unsuccessful, however it has warranted further investigation into the overall effectiveness of the system for fault detection.

APPROVAL PAGE

The faculty listed below, appointed by the Dean of the School of Computing and Engineering, have examined a thesis titled "Strain Gauge Utilization for Aerial Vehicle Dynamic Load Measurement," presented by John Bazin, candidate for the Master of Science degree, and hereby certify that in their opinion it is worthy of acceptance.

Supervisory Committee

Travis Fields, Ph.D., Committee Chair
Department of Civil & Mechanical Engineering

Antonis Stylianou, Ph.D.
Department of Civil & Mechanical Engineering

Gregory King, Ph.D.
Department of Civil & Mechanical Engineering

CONTENTS

ILLUSTRATIONS

TABLES

List of Abbreviations

$\{a_{x,meas}, a_{y,meas}, a_{z,meas}\}$	=	Acceleration scalars measured from the onboard acceleration, $[m/s^2]$
${}^N\underset{\rightarrow}{\mathbf{a}}^{BC}$	=	Acceleration vector of the vehicle at the center of rigid body B location in the Newtonian frame, $[m/s^2]$
${}^N\underset{\rightarrow}{\mathbf{a}}^{M}$	=	Acceleration vector of motor M in the Newtonian frame, $[m/s^2]$
$\{\hat{\mathbf{b}}_x, \hat{\mathbf{b}}_y, \hat{\mathbf{b}}_z\}$	=	Dextral orthogonal unitary basis fixed to vehicle frame
b	=	Quadcopter motor damping constant
c	=	Line Convergence Factor
DF	=	Design Factor
e	=	Abrasion Loss Factor
$F_{t,meas}$	=	Total measured load, [N]
$F_{t,sum}$	=	Sum of Suspension Line Loads, [N]
F^M_{meas}	=	Measured force at motor M location, $[N]$
F^M_{thrust}	=	Thrust force from motor M, $[N]$
g	=	Acceleration due to gravity, $[m/s^2]$
I	=	Quadcopter inertia, $[kg * m^2]$
K	=	Quadcopter motor torque constant, $[\frac{1}{s^2}]$
k	=	Fatigue Factor
m	=	Dynamic load Factor
m^M_{eff}	=	Effective mass for aircraft arm with motor M, $[kg]$
$\{\hat{\mathbf{n}}_x, \hat{\mathbf{n}}_y, \hat{\mathbf{n}}_z\}$	=	Newtonian (inertial) dextral orthogonal unitary basis
o	=	Environmental Conditions Factor
$\{q_{rx}, q_{ry}, q_{rz}\}$	=	Euler angles of the vehicle with rotational order roll-pitch-yaw, $[rad]$
$\{q_{tx}, q_{ty}, q_{tz}\}$	=	Translational generalized coordinates following North-East-Down positive directions, $[m]$

$\{\dot{q}_{rx}, \dot{q}_{ry}, \dot{q}_{rz}\}$	=	Traditional angular velocity scalars of the aircraft, $[rad/s]$
$\{\dot{q}_{tx}, \dot{q}_{ty}, \dot{q}_{tz}\}$	=	Traditional translational velocity scalars of the aircraft, $[m/s]$
L	=	Quadcopter arm length $[m]$
R_{1-4}	=	Strain gauge resistors $[\Omega]$
$Roll_{CMD}$	=	Quadcopter motor roll command
$\underset{\rightarrow}{\mathbf{r}}^{M/BC}$	=	Position vector from the center of rigid body B motor M, $[m]$
s	=	Asymmetrical Suspension-Line Load Distribution Factor
SF	=	Safety Factor
t_p	=	Temperature Degradation Factor
TTC	=	Time for motor torque constant to converge after failure, $[sec]$
u	=	Joint Loss Efficient Factor
$\{U_1, U_2, ..., U_6\}$	=	Generalized speeds (1-3 are rotations, 4-6 are translations) used in creation of Kane's dynamics equations, $[rad/s, m/s]$
V_o	=	Wheatstone bridge voltage output $[V]$
V_{EX}	=	Wheatstone bridge voltage excitation $[V]$
${}^N\underset{\rightarrow}{\boldsymbol{\alpha}}^B$	=	Angular acceleration of the vehicle B in the Newtonian frame, $[rad/s^2]$
ϵ	=	Least Squares regression equation error
${}^N\underset{\rightarrow}{\boldsymbol{\omega}}^B$	=	Angular velocity of the vehicle B in the Newtonian frame, $[rad/s]$

ACKNOWLEDGEMENTS

I would like to thank the University of Missouri-Kansas City Summer Undergraduate Research Opportunity Program (SUROP) and the Students Engaged in Artistic and Academic Research (SEARCH) program for their funding in parts of this thesis. I would also like to acknowledge Nicolas Basore, Ignacio Hernandez, Caleb Chase, Logan Ellis, Andrew Reardon, Dan McCullough, Mohommad Alabsi and John Smith for their assistance during drop testing events, flight testing events, and software development.

I would also like to thank my academic advisor Dr. Travis Fields, who co-authored all of my conference publications. He has played an instrumental roll in all of the research and development efforts presented in this thesis.

I would like to thank my family for their support and encouragement.

CHAPTER 1

INTRODUCTION

1.1 Background

Strain gauge development has been an essential part of the engineering community since the mid 1900s [47]. They are still used today for a wide variety of applications as well as in new technological innovations. Some technological innovations that will be expanded on in this thesis are related to aerial vehicle dynamics and measurement. Specifically, aerodynamic decelerator systems (parachute) inflation profile and quadrotor thrust force estimation applications will be investigated for incorporation of strain gauge instrumentation. Historically, strain gauges are used in conjunction with a variety of other instrumentation to achieve or deliver a dynamic measurement of some sort [35]. In the case of this thesis, strain gauges will be used in an effort to create different types of force transducers aiding in the understanding of both circular parachute and quadrotor behavior.

Circular parachutes have been used for centuries. The first recorded design for a general parachute was documented in the late 1400s [53]. An anonymous drawing depicted a free-hanging man clutching a cross bar frame attached to a conical canopy can be seen in Figure 1 [53].

Leonardo da Vinci is also credited with some of the first parachute designs in the early 1500s. The modern parachute was developed in the late 1800s by Louis-Sebastien [53]. Since then, parachute design has improved and grown into a large industry with

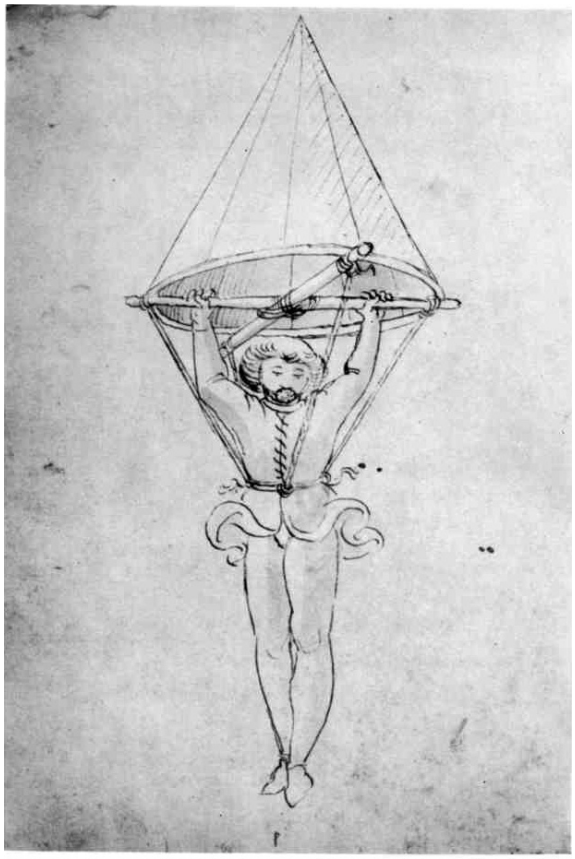

Figure 1: Anonymous drawing of first parachute [53]

different types and styles of canopies. Such topics in this industry that are still studied include reefing techniques, NASA Mars rover landings, and atmospheric reentry vehicles [10, 17, 34].

The concept of the multirotor aerial vehicle has been around since 1907 when the first four-rotor helicopter lifted itself off of the ground [57]. The first quadrotor was designed by Louis Berguet, and only flew a few feet. The first successful multirotor design was the “de Bothezat helicopter“ named after its inventor George de Bothezat seen

in Figure 2 [57].

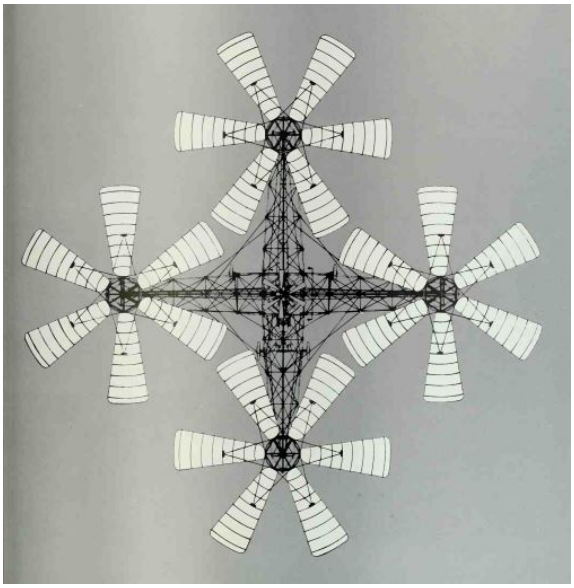

Figure 2: First quadrotor aerial vehicle design drawing [57]

The concept of the unmanned aerial vehicle (UAV) became relevant for fixed wing aircraft with military drones. Over the past few decades there has been a resurgence of multirotor aircraft, specifically with small multirotor UAVs [37]. The need for maneuverable aircraft with hovering capabilities has led to this increase in research and development. The quadrotor design is a simple, yet reliable and highly maneuverable. The applicability of multirotor UAVs is vast, with a sampling of current applications including search and rescue, land surveying, and crop inspection [23, 37, 39].

1.2 Motivation

The motivation behind this thesis stems from the interest in expanding strain gauge measurement technology in aerospace applications. Strain gauges are a common tool used in the engineering community for their versatility and low-cost. The very broad topic of dynamic load measurement is where the strengths of using strain gauges lies due to their ability to be utilized in a such a wide range of applications. The work presented herein has been performed in an effort to improve the dynamic measurement capabilities of aerial vehicles through incorporation of strain gauges and appropriate modeling/correction software.

Suspension line load measurement for all types of aerodynamic decelerators is an area that has been researched for decades [36]. However, many studies focus on suspension line elasticity and oscillation frequency under loading rather than focusing on suspension line loading pattern behavior leading to canopy deformation [42]. An important aspect of understanding parachute deformation behavior is the quantification of suspension line load distribution experienced in circular parachutes upon inflation and during terminal descent. A better understanding of suspension line loading patterns could aid in the development of autonomous parachute vehicles with high landing accuracy. NASA has been interested in such vehicles for moon and mars rover landings [10]. A current limiting factor in controlled circular parachute landing accuracy is the lack of understanding of the effects of deforming the parachute on the canopy (i.e. symmetric deformation inducing horizontal motion). Although not traditionally studied, there has been research in the area on parachute suspension line loading patterns. A study was performed in 2011

in which NASA flight tested the first two generations of the orion parachute program [34]. The NASA study was performed in a effort to observe potentially significant suspension line loading patterns of the orion parachutes. NASA was able to observe significant asymmetric suspension line loading patterns, warranting further investigation into the topic of asymmetry and its effect on circular parachute suspension line loading. Significant asymmetric loading patterns in circular parachutes is an important aspect to take into account when designing parachute suspension lines due to the dynamic load seen by each suspension line. NASA created a successfull load distribution mesurement system in order to observe the suspension line loading, but the system exhibited difficulties in data processing. Each of NASA's suspension line load cells did not wirelessly send data, to time syncing flight test data was tedious. A study was performed in this thesis that eliminates this issue by wirelessly sending data from each suspension line load cell to a host device. The previous study performed by NASA provided the framework and fundamental testing methodology techniques that led to the pursuit of the first objective in this thesis.

Expanding on the strain gauge technology developed for parachute testing, a method is described in this thesis that that uses them in the estimation of quadcopter UAV thrust in real-time. The research and development of quadcopter UAVs is something that is ongoing and has increased in popularity over the past two decades. However, a current limiting factor preventing an even more rapid growth in small UAV use are the accident rates associated with them. Instances in which small unmanned aerial vehicle have crashed into public places has increased substantially over the past several years due to inexperienced pilots, mechanical failures, and software failures [48,49]. The number of accidents

involving UAVs can be reduced with the development of more fault tolerant flight controllers. A requirement of fault tolerant control for a quadcopter UAV is the ability to detect and mitigate failures during flight. Currently, fault tolerant control techniques involve different types of state observers for fault detection which does not provide a direct measurement of the parameters that could cause a failure in a quadcopter system. [3, 56]. The utilization of strain gauges for in-flight thrust estimation has not been addressed in literature, and has the potential to aid in the development of a robust flight controller. The advantages of such a system include: quick failure detection, minimal computation time, and insensitivity to noise.

1.3 Thesis Objectives

1. Develop and evaluate a circular parachute strain gauge-based load distribution measurement system.

2. Develop and evaluate strain gauge-based thrust estimation system on a quadrotor aerial vehicle.

3. Compare the strain gauge-based thrust estimation system with an indirect real time parameter estimation technique for motor fault detection.

1.4 Thesis Organization

The work presented herein is organized into four chapters as follows. Chapter 1 is a brief overview into the significance of aerodynamic decelerator research in relation

to strain gauge technology as well as the significance of using in-flight quadrotor motor thrust estimation in conjunction with a feedback control system in a flight controller. Chapter 2 provides a detailed background of strain gauge technology being used for load measurement, aerodynamic decelerator research and significance, and the significance of using in-flight quadrotor motor thrust estimation. The bulk of the study information is contained in Chapters 3,4, and 5 including detailed study methodology, results obtained, and a discussion of the overall outcome. Chapter 6 presents a conclusion of the research study, including interpretation of obtained results, comparison to previous studies, implications of the findings, limitations of the current study and suggestions on future work.

1.5 Conference Proceedings

The work developed was published in the conference proceedings below. The first publication (Chapter 3) was a student paper finalist for the 23rd AIAA Aerodynamic Decelerator Systems Technology Conference and Seminar, the second publication (Chapter 4) was presented at the AIAA SciTech conference in San Diego, California, and the third publication (Chapter 5) received 3rd place in the master's degree category at the AIAA Region V student conference in Ames, Iowa.

- Bazin, J.M. and Fields, T.D., Validation and Flight Testing of a Wireless Load Distribution Measurement System. *23rd AIAA Aerodynamic Decelerator Systems Technology Conference and Seminar*, March 30 - April 2, 2015, Daytona Beach, Florida.

- Bazin, J.M. and Fields, T.D., Feasibility of In-Flight Quadrotor Individual Motor

Thrust Measurements. *AIAA Science and Technology Forum and Exposition*, January 4-8, 2016, San Diego, California.

- Bazin, J.M. and Fields, T.D.,A Comparative Study Between Real-Time Parameter Estimation and Strain Gauge-Based Estimation for Quadcopter Rotor Failure Detection. *AIAA Region V Student Conference*, April 6-8, 2016, Ames, Iowa.

CHAPTER 2

LITERATURE REVIEW

2.1 Strain Gauge Use and Development

Strain can be described as the amount of deformation of a body due to an applied force in comparison to the original formation of the body. Strain can be a positive or negative quantity and can be measured using many different techniques including: bending force on a metal bar, axial force on a metal bar, and tension in a cable [35]. One of the most commonly used strain gauges is the thin film strain gauge. The thin film strain gauge's electrical resistance varies in proportion to the amount of strain in it. A thin film strain gauge is often manufactured with a conductive material. A thin film strain gauge consists of a fine wire or metallic foil arranged in an accordion-like pattern. The purpose of arranging it in an accordion-like pattern is to allow for a sufficient amount of material while at the same time being insensitive to off-axis effects. Thin film strain gauges are available commercially and with their resistance values varying from 30 to 3,000 Ω [35]. In general, the quantity of strain measurements are incredibly small values, and therefore require an accurate measurement of a change in resistance. In order to receive the change in resistance in a usable form, thin film strain gauges are often used in a Wheatstone bridge configuration with four strain gauges and an excitation (Figure 3).

In Figure 3, four thin film strain gauges are represented as resistors. Gauges R_1 and R_3 represent the gauges on the top of the beam, and gauges R_2 and R_4 represent the

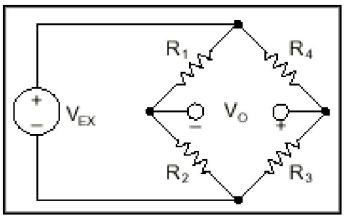

Figure 3: Full Wheatstone bridge configuration [35]

gauges on the bottom of the beam. The output voltage V_o can be determined from the Wheatstone bridge with Equation 2.1 [35]. When a force is applied to a beam with the full Wheatstone bridge configuration (four strain gauges) described in Figure 3, the output voltage will increase or decrease linearly in proportion to how much strain the beam is experiencing. This linear relationship can then be related to a linear change in force using standard calibration techniques [1].

$$V_o = [\frac{R_3}{R_3 + R_4} - \frac{R_2}{R_1 + R_2}] \cdot V_{EX} \tag{2.1}$$

Strain gauges are currently being utilized in the engineering community for research and commercial applications. The attraction to the use of the strain gauge comes from the fact that they are inexpensive and accurate. However, strain gauges can be tedious to apply and tend to be fragile. Strain gauges have aided in many engineering research problems in the past two decades in such subjects as botany, biomechanics, and micro mechanics, specifically measuring the change in fruit diameter over a long period of time, inexpensively measuring intracranial pressure, and measuring the wing force on a micromechanical flying insect.

An improved strain gauge device was created for continuous field measurement of stem and fruit diameter to replace old, outdated measurement tools that do not have the capability requirements needed for a proper analysis [46]. The fruit diameter measurement device created was the dendrometer DEX70. The DEX70 is similar to previous dendrometers made in the 1980s, but is more flexible which allows for a greater change in thickness before a physical reset is required. The DEX70 is made out of two aluminum bars attached to a stainless steel band on which the strain gauges are attached. Four strain gauges are attached created a full Wheatstone bridge circuit configuration. The most important part of the full Wheatstone bridge configuration is the temperature compensation gained, which is anticipated to change due to weather variation as the fruit grows.

A strain gauge microsensor was developed in the field of biomechanics for measuring intracranial pressure (ICP) in the intraventricular space. This sensor was tested against two other traditional, invasive measurement techniques and showed that there was no significant difference in the mean ICP readings. In "A Clinical Study of Parenchymal and Subdural Miniature Strain-Gauge Transducers for Monitoring Intracranial Pressure," Intracranial pressure was measured using a subdural microsensor catheter that was inserted into a ventriculosomy catheter [51]. This was locked into position so that the strain gauge was located 1 cm away from the tip of the ventriculosomy catheter. The study resulted in successful, accurate ICP readings from the new strain gauge-based method [51].

In a more relevant topic to this thesis, a study was performed that "describes aspects of the Micromechanical Flying Insect (MFI) in the areas of mechanical design and fabrication, actuation and sensing, and wing control" [50]. In this study, strain gauges

were used in a small portion of the project for wing force measurement, but still played an important roll in the development of the MFI. Wing force measurement came from using semi-conductor strain gauges mounted directly on the wing spars. The measurements from these gauges served two purposes. They gave initial off-line characterization of forces generated during wing motion and eventually gave feedback in the real-time wing control system [50]. However, inertial forces were not compensated for during free flight which could prove problematic for the feedback in real-time.

These systems have demonstrated the use of strain gauges in the area of dynamic load measurement. This thesis, at its core, is a demonstration of the use of strain gauges to aid in the dynamic load measurement in two specific applications. The first system uses strain gauges to aid in load distribution measurement for circular parachutes after the proper calibration and software configuration. The second system uses strain gauge measurements on a small multirotor unmanned aerial vehicle to aid in the model development of an individual motor thrust estimation system.

2.2 Aerodynamic Decent Vehicles

One of the first aerodynamic decelerator systems recorded in history was the parachute. Parachute design dates back to the early 1500s with one of the first initial sketches described by the inventor Leonardo de Vinci [53]. The concept of the parachute was put into practice in the early 1900s with one of the first experiments performed by throwing a dummy off of the Eiffel tower [30]. The development of parachutes has been a growing industry since then, with advancements in multiple aspects of their design. ”The

Knacke parachute design manual" is the guide to fundamental parachute design [27]. The first objective of this thesis focuses on the study of circular parachute asymmetric canopy loading. Asymmetric canopy loading is an area of circular parachute behavior that has not been traditionally studied, but has been acknowledged in the parachute community and the Knacke Parachute Design manual [27, 34]. Traditionally, parachute canopy loading has assumed to be symmetric or that asymmetric canopy loading can be neglected. Research has been performed in which total load measurements of circular parachute suspension lines upon inflation and terminal descent has been performed for a better understanding of parachute loading behavior [12, 33]. Techniques have been researched to improve landing accuracy of circular parachutes by investigating reefing techniques [19] Individual suspension line load measurement is a relevant aspect of the study of circular parachute behavior even though it has not been traditionally studied or focused on. The strength of suspension lines under dynamic loading for circular parachutes has been studied and dates back to the 1970s [36]. The study of suspension line strength under dynamic loading concluded that further research was needed in the area of material response under oscillatory loadings [36, 42]. Such studies have been relevant for the past four decades as new developments in oscillatory response of suspension lines continue to be researched today [42]. Oscillatory response of suspension lines is studied today in an effort to better understand the material deformation that may occur to parachute suspension lines during critical moments of descent. The study of asymmetric canopy loading may be helpful in better understanding oscillatory behavior of circular parachute suspension lines during dynamic loading. The first objective of this thesis expands on

two studies in which asymmetric canopy loading of circular parachutes is investigated by developing a new, non-invasive, wireless load measurement system [17,34]. The previous studies performed by NASA and UMKC provided the framework for the first objective of this thesis, providing the testing methodology and proper background to create a unique load measurement system [17, 34].

2.3 Multirotor Unmanned Aerial Vehicle Development

The concept of the multirotor has been around since the early 1900s with the invention of the first quadrotor aerial vehicle by Louis Berguet [57]. Though Burguet's quadrotor only flew for a few feet, it was still an achievement that was later to be expanded on. The first successful multirotor design was the "de Bothezat helicopter" named after its inventor George de Bothezat seen in Figure 2 [57]. The Bothezat quadrotor had its first flight in 1922 and had more than 100 successful flights after. Bothezat was a Russian scientist who constructed the quadcopter under a United States Army contract. Bothezat's contract was terminated in 1924 and the quadcopter was scrapped due to its inefficiency, complexity, and difficulty to pilot [57].

The next major quadrotor was invented in the 1950s along with the traditional helicopter design seen today with only two rotors [14] [57]. The quadrotor, known as Convertawings Model A, was designed with military purposes in mind, but lacked interest due to the invention of the modern helicopter [14]. An important part of Convertawings Model A was the implementation of variable thrust in each of the four motors, which is the primary control scheme used in current quadrotor aircraft. However from the 1950s

on, most technological efforts for rotorcraft focused on improving the single primary rotor design, or modern helicopter, until technological advancements came about that allowed for the development of small-scale unmanned multirotors.

The new millennium brought about advancements in electronics that allowed for the production of small, lightweight flight controllers. Inertial Measurement Units (IMU), Global Positioning Systems (GPS), lithium polymer batteries, and high quality cameras directly contributed to the rapid growth in interest in small multirotor unmanned aerial vehicle (UAV) [25]. One of the most important aspects of designing a multirotor UAV is the implementation of a robust, fault tolerant flight controller. There are many different approaches to designing a flight controller. The research presented in pursuit of the second and third objectives of this thesis are meant to assist in the future development of a fault tolerant flight controller by investigating new ways of estimating time variant and time invariant aircraft parameters. Currently, many types of adaptive flight controllers use state observers for their parameter estimation [3, 56]. A typical state observer provides an estimate for an internal state of a system by observing the measurements of the input and output of the real system. Using state observers for parameter estimation can be performed in real time, however it is not a direct measurement of the system. A direct measurement technique in parameter estimation could potentially prove useful for fault detection because of the potential to detect a failure quickly. One challenge with real time parameter estimation is finding a technique that is insensitive to noise, but can still detect a failure, or signifiant parameter change, quickly enough for a controller to potentially mitigate the anomaly [32]. The work presented in pursuit of the second and third

objectives of this thesis focus on a unique strain gauge-based thrust estimation system. The incorporation of a the strain gauge into a fault tolerant flight controller has not traditionally been seen in literature, but could potentially provide a unique solution to the challenge in parameter estimation of finding a technique that is fast and yet insensitive to noise.

2.4 Flight Testing

2.4.1 Aerodynamic Descent Vehicle Testing

An important aspect of the first objective in this thesis is the testing procedure used in comparison to standard descent vehicle practices. Modeling parachute behavior can be difficult due to the unpredictability of wind and airspeeds during drop testing. The US Army Natick Soldier Research Development and Engineering Center (NSRDEC) developed indoor testing regimen that produced repeatable and consistent parachute performance data such as canopy deformation patterns for computer simulation validation. [13]. The testing regimen involved using a guided vertical drop system in a controlled environment. A steel guide wire was anchored to the floor of the structure and extended vertically through the centerline of the payload and the vent of the canopy to the ceiling. A sketch of this testing setup can be seen in Figure 4.

The guide wire eliminated rotation and increased repeatability for the heavily instrumented payload [13]. A static line was used to allow the parachute to fall for a period of time determined by the length of the static line in these experiments before being allowed to inflate. The static line was attached to a deployment bag in which the parachute

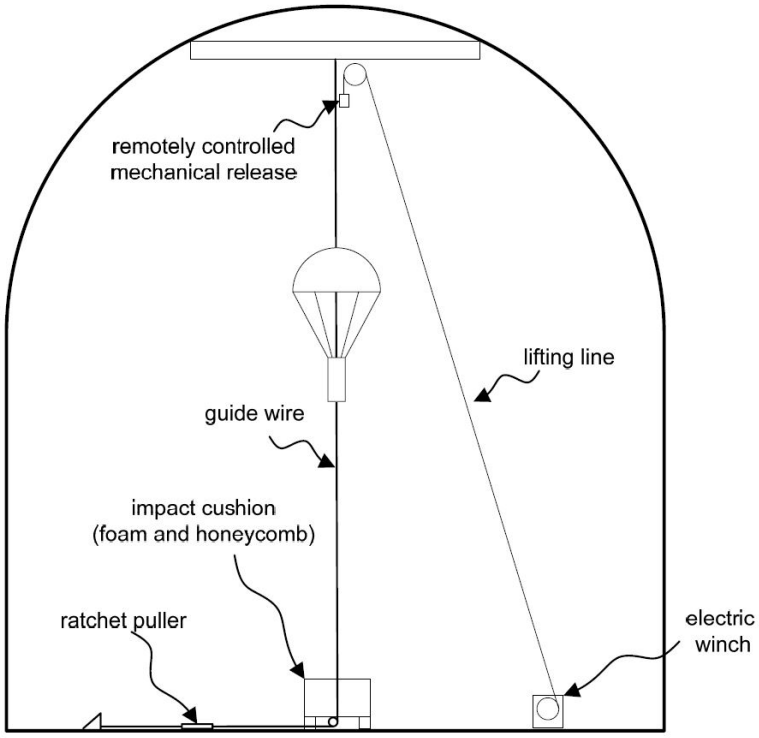

Figure 4: NSRDEC indoor parachute drop testing setup [13]

was packed. The use of a static line attached to a deployment bag induces a snatch load once the parachute breaks free from the deployment bag, which simulates actual inflation events during actual aerial delivery operations. The use of static lines attached to deployment bags is a standard practice when performing parachute drop tests as it is also seen in outdoor drop testing procedures [27,29]. The drop testing procedure used in pursuit of the first objective in this thesis is modeled after the NSRDEC testing procedure for accuracy and repeatability.

2.4.2 Multirotor Unmanned Aerial Vehicle Testing

Multirotor unmanned aerial vehicles are often tested indoors in closed, safe environments while using precision location instrumentation. During the testing development of a flight controller, the test multirotor often will exhibit unpredictable movements that can cause injuries if the proper precautions are not taken. Indoor flight testing is also legal under FAA regulations and also allows for the use of precision location instrumentation such as motion capture systems. Motion capture systems can be used for a number of different applications in the area of multirotor system identification, but tend to be very cost inefficient and are tedious to assemble [45]. Motion capture systems are commonly used for position translational data because most instrumentation feedback requirements can be met with on-board sensory (i.e. rotational displacement or attitude). There have been efforts to improve the cost efficiency of motion capture by using less expensive cameras as well as on-board cameras [4, 28, 45]. A study was also performed that focused on improving current motion capture feedback and accommodating for position drift due to physical deformities [16]. Often in multirotor flight tests in which motion capture is used, the marker arrangement tends to change slightly, but altering position feedback. This tendency to drift can also occur in the camera positions themselves. A method was developed that accommodates for any offset in the attitude measurements resulting in better flight performance [16]. Motion capture usage in the testing of multirotor vehicles is useful for feedback information when developing flight controllers, with new developments in the area being explored. Chapter 4 takes a unique approach to using a motion capture system while testing multirotor unmanned aerial vehicles by using rotation data as well

as traditional position and altitude measurement.

CHAPTER 3

VALIDATION AND FLIGHT TESTING OF A WIRELESS LOAD DISTRIBUTION MEASUREMENT SYSTEM

This information can be found in the conference proceedings of the 23rd AIAA Aerodynamic Decelerator Systems Conference and Seminar, Daytona Beach, Florida

3.1 Introduction

Aerial delivery systems are currently being deployed globally for a variety of aerial resupply applications with a wide range of parachute-payload designs. Autonomously controlled circular parachute systems and autonomous ram-air parafoil systems have been developed to improve landing location accuracy over uncontrolled circular parachute aerial deliveries. Ram-air parafoils have proven capable of tremendous landing location through development and implementation of sophisticated trajectory generation and tracking algorithms [43, 44, 52]; however, the cost of such systems have limited the applicability in modern combat scenarios [8]. Autonomous circular parachute systems have shown promise for reducing aerial delivery costs, but have been unable to achieve suitable landing location accuracy. Two fundamentally different approaches to circular parachute control have been developed: asymmetric canopy deformation and symmetric canopy deformation. Asymmetric canopy deformation utilizes asymmetric suspension line loading to produce a small glide slope [15, 55]. Symmetric canopy deformation incorporates a reversible reefing system to manipulate descent time in a known wind column to control

the landing location [18–21]. Currently, a limiting factor in controlled circular parachute landing accuracy is the lack of understanding of the effects of deforming the parachute on the canopy (i.e. symmetric deformation inducing horizontal motion). One aspect of understanding parachute behavior is the quantification of the suspension line load distribution experienced in circular parachutes upon inflation and during terminal descent. A recent study conducted in 2011 presented loading information measured from the bridle of the Orion parachute system [34]. The purpose of the study was to investigate canopy asymmetric loading. Flight test results demonstrated significant asymmetric canopy loading during numerous drop tests. The major drawback of the Orion parachute load distribution measurement system was the requirement of suspension line loading data to be time synced while post processing the data. This led to a tedious testing regimen as well as well as time consumption.

There has been widely spread interest in developing autonomous parachute vehicles over the past 20 years [8]. NASA has been in need of such vehicles for moon and mars rover landings [10]. By incorporating a canopy load measurement system during the flight testing design phase, a safer and more accurate aerodynamic decelerator can be developed. A system which could provide suspension line and/or control line loading data for a much more wide variety of parachute/payload configurations that are directly related to current delivery system efforts. To be readily applicable to the various autonomous descent vehicles (parafoil, asymmetric deformation, and symmetric canopy deformation), the developed load distribution measurement system wirelessly transmits data thereby enabling load cell mounting anywhere on the suspension/control line. Additionally, the

developed load distribution system incorporates a suspension line load cell that can be rapidly installed onto any suspension line without line modification. The wireless, noninvasive system can be quickly and easily deployed on any aerial delivery vehicle system.

A recent study demonstrated feasibility of the wireless load distribution measurement system [17]. This system contained a custom non-invasive load cell design and amplification board. The custom load cell design was improved upon through two design iterations combined with the use of basic finite element analysis. The custom strain gauge amplification unit proved difficult to maintain zero and constant calibration. Additionally, the measurement system was capable of measuring parachute load distribution at a maximum sampling rate of 50 Hz, resulting in low resolution during canopy inflation.

This paper describes an redesigned signal conditioning system that integrates a software-controlled auto-bias algorithm, and an increased sampling rate. The paper is organized as follows: Section 3.2 describes the load cell design, signal conditioner development, and testing methodology. Section 3.3 provides and discusses flight testing results for custom load cell verification, asymmetric canopy loading, and induced effects of the suspension line load cells. Finally, Section 3.4 summarizes and concludes major results from the study, and presents measurement system limitations.

3.2 Methodology

3.2.1 Load Cell Design

A custom load cell was designed to accommodate a variety of payload weights. The load cell design can be manufactured with a single aluminum sheet inexpensively

and quickly. The custom load cell used in this study was originally developed from the load distribution feasibility study [17]. As seen in Figure 5, the upper end of the load cell is rigidly attached to the suspension line, which then passes over the strain gauge (half-bridge configuration) instrumented cantilever and through a suspension line guide hole, making an ”E” shape. This custom load cell is machined from a single 3.2mm (0.125in) thick piece of aluminum. The load cell was calibrated to have a rated capacity of 15N (3.4lbs). Finite element analysis was used to provide validation for the initial design; however, due to inherent complexities in designing load cell geometry [5], experiment-based tuning was used to determine the final design (as is typical load cell design) [9].

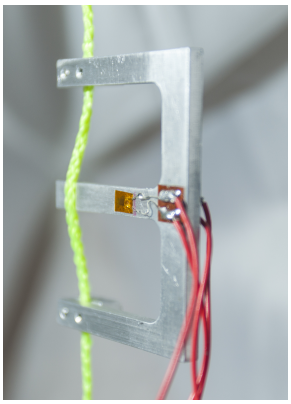

Figure 5: Custom strain gauge load cell design.

3.2.2 Signal Conditioner Design

A custom printed circuit board (PCB) was designed and assembled to convert the small resistance change of the load cell strain gauges into a usable form for a microcontroller's 10-bit A/D converter to sample. This signal conditioning board (seen in Figure 6) uses a Wheatstone bridge circuit to measure the change in resistance from the deflecting

strain gauges, and then convert it to a change in voltage. The voltage is then amplified with an instrumentation amplifier (Analog Devices AD 623) which converts the small voltage to a more usable range that can be easily sampled by the low-resolution microcontroller. A digital potentiometer (Analog Devices AD5272) was also implemented into this design to enable a software-based bias control of the Wheatstone bridge output voltage. Each time the device is powered up, the software bias control adjusts the digital potentiometer to ensure the most accurate readings for each drop test. For visual verification, two light emitting diodes (LED) were added and programmed to signal the user when the PCB and microcontroller were ready for data collection, and that the load cell has been properly calibrated with the automated bias control.

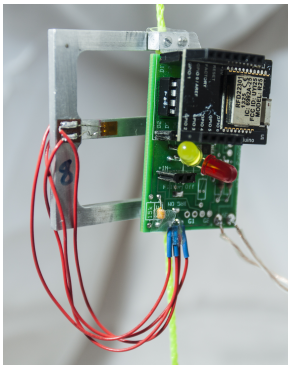

Figure 6: Load cell with conditioner PCB.

Each signal conditioning board utilizes a RFduino microcontroller for all computations and wireless communications. The RFduino runs on the easy-to-use Arduino programming operating system and has six general purpose inputs and outputs, 16MHz ARM Cortex processor, 2.4GHz built in Bluetooth, 128kb flash memory, and 8kb RAM.

Using the built-in Bluetooth Gazelle network, each RFduino transmits the measured suspension line load to a host RFduino (housed in the payload section) at a rate of 500Hz (20 samples sent per transmission). Previous efforts with this design yielded a maximum sampling rate of 50Hz (three samples sent per transmission). The significantly faster sampling rate was achieved by modifying the low-level Gazelle network firmware. The RFduino can be seen on the signal conditioning board shown in Figure 6 (small silver box). The complete load cell/conditioning board with lithium battery has a mass of 24.6g (0.87oz). The individual component masses are shown in Table 1.

Table 1: Single suspension line load measurement system mass by component.

Component	**Mass (Grams)**
3.7V Lithium Battery	3.04
PCB	9.49
Custom Load Cell	7.28
Rfduino	4.80
Total	24.6

The slow sampling speed limiting the previous feasibility study [17] was found to be the result of the Gazelle network's significant overhead and syncing issues encountered between the device and host wireless communication. The Gazelle protocol continuously cycles through six channels, which reduces interference issues at the loss of throughput and consistency. To overcome the loss of throughput, a single, static channel per device was used. Bench testing of the single-channel/device resulted in a system that required more time to switch channels than to actually send the load cell data. A packet size of 20 load samples (per device) was implemented, to improve overall throughput efficiency. To keep everything in sync at a transmission rate of 25 Hz (sampling rate of 500 Hz), the host

device pings each client until they are all plugged in and calibrated. Once this happens the host sends a countdown to the devices, which compensates for communication latency and already elapsed time, allowing the devices to begin sampling at the exact same time (accuracy limited to the 16MHz clock speed of the microcontroller).

3.2.3 Testing Methods

A static calibration of the custom load cells was performed prior to drop testing the complete load measurement system. Each load cell was attached to a Bose ElectroForce 2200 load frame via nylon string. The nylon string acted as the suspension line for the load cell, with one end fixed to the Bose Frame, and the other attached to a Bose load cell (providing a known force measurement). One custom load cell attached to the Bose frame can be seen in Figure 7 (left). Each load cell was calibrated in accordance to standard calibration procedures [1, 5] with two trials performed for each individual load cell. A total of five load cells were calibrated using this procedure. Four individual suspension line load cells, denoted $LC_1 - LC_4$, were calibrated to a load cell rating capacity of 15N (3.7lbs). The fifth custom load cell, denoted LC_T was calibrated to an load cell rating of 60N (13.5lbs). During parachute drop testing, the higher rated load cell and was placed below the suspension line confluence point in order to provide a total canopy load measurement. The total load measurement was used for validation of the custom load cells. For the four suspension line rated load cells, $LC_1 - LC_4$, the average hysteresis was 8.0% of the rated capacity with an average repeatability error of 0.6% of the rated capacity. The fifth load cell had a hysteresis of 8.0% of the rated capacity with a repeatability error

of 0.8% of the rated capacity. One loading cycle for a single 15N (3.7lbs) load cell is shown in Figure 7 (right).

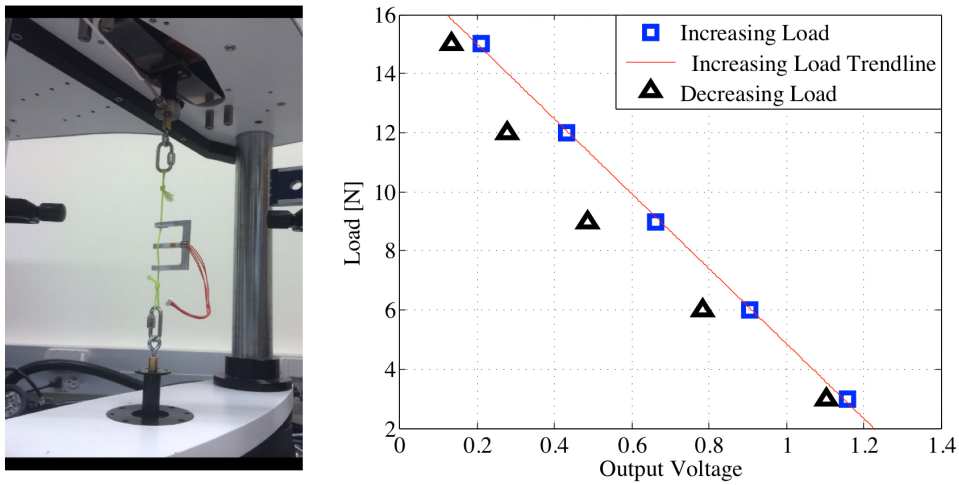

Figure 7: Load cell calibration test apparatus (left) and single trial from load cell calibration with trend line of increasing load cycle (right).

Drop testing was performed with a 1.2m (4.0ft) quarter-spherical cross-based parachute with a payload 2.0kg (4.4lbs). Drop testing was performed indoors from a stable drop height of 12m (39ft). A guide line was used to improve repeatability by reducing effects caused by canopy/payload rotations. Drop testing was conducted with a 0m and 1.8m (6.0ft) static line to investigate the different velocities and inflation times associated with the two static line scenarios. A servo actuated release mechanism was designed and programmed to release the parachute/payload when desired via a remote-control transmitter held by the flight test coordinator. Suspension line load data was collected from four load cell/signal conditioners mounted onto each suspension line (four suspension lines total), corresponding to the four load cells, $LC_1 - LC_4$ discussed previously. To validate the

load cells, the summation of the individual load cell data, LC_{sum}, was compared against data collected from a single load cell mounted below the suspension line confluence point, LC_T. The inflation sequence for a zero-length static line deployment test can be seen in Figure 8.

Figure 8: Inflation sequence during a zero-length static line deployment.

Asymmetric loading has not been traditionally studied or observed due to symmetric assumptions, but has been taken into account during parachute design. Knacke's Parachute Recovery Systems Design manual [27] contains an equation for calculating a parachute design factor:

$$DF = SF(mcs/uekot_p) \tag{3.1}$$

All inputs in the numerator(m, c, and s) represent unknown loading factors, one of which is the Asymmetrical Suspension-Line Load Distribution Factor, s. Traditionally,

Knacke's design manual uses an asymmetrical load factor or 1.0 or 1.1. An asymmetric load factor of 1.1 is still the standard used for current parachute design practice [27, 33, 34]; however, the Ares Asymmetrical Loading and Design Recommendations study and the Crew Exploration Vehicle Parachute Assembly System study have measured loading factors greater than 1.1 [33, 40].

Quantifying the effects of the load cells on parachute flight dynamics was accomplished by performing drop testing with a single load cell at the suspension line confluence point (LC_T) along with the use of a barometric presser transducer housed in the payload. Investigation of the suspension line load cells was studied because of the potential for the each load cell to dramatically modify the parachute behavior (increase inflation time, alter peak load, etc.). Drop testing data collected without the suspension load cells mounted were compared to identical testing conducted with the suspension line-mounted load cells($LC_1 - LC_4$) attached to each suspension line. Multiple drop tests were performed to quantify scatter in data from a single drop scenario and compared with drops performed without suspension line-mounted load cells to estimate load cell impact on parachute behavior.

3.3 Results & Discussion

Testing was performed resulting in a total of 12 drop test data sets that are used to validate the load distribution measurement system, quantify load asymmetry during inflation and terminal descent, and quantify effects of the mounted suspension line load cells on the overall parachute behavior. A 1.8m (6ft) static line was used for six drop tests

and a 0m static line was used the remaining six drop tests. Within each static line drop test scenario, three tests were conducted with the custom load cells mounted to the suspension lines, and three tests conducted without the custom load cells. All drops were conducted using a payload weight of 2kg (4.4lbs). Peak inflation loads ranged from 30.6N - 54.1N. Terminal velocities ranged from 5.46 m/s - 6.06 m/s for 0m static line tests, and 6.19 m/s - 7.31 m/s for 1.8m (6ft) static line tests. A summary of these findings can be found below.

3.3.1 Load Cell Verification Results

Figure 9 demonstrates system validation for 0m (left) and 1.8m (right) static line drop tests for one of the three drop tests in each configuration. The sum of the load cells, LC_{sum}, on the suspension lines shows a peak load greater than the total measured load. The difference between the peak load can be partially attributed to the weight of LC_T load cell as well as a line-separator ring added immediately above the LC_T load cell to aid in minimizing suspension line tangling. The 0m static line shows an average peak load of 36.95N and the 1.8m (6ft) static line shows an average peak load of 40.53N. The total load measurement data from the third 0m static line drop test (Table 2) is not used in average calculations because it is deemed an out-liar when compared with all of the tests conducted. The average peak load results exhibit a small separation due to impact of the difference in velocity at the time of inflation (caused by the two different static line lengths). The longer static line produces a higher descent velocity at the time of inflation, thereby increasing the peak inflation load and reducing the inflation time. The expected load at terminal velocity should equal only the load due to payload weight (19.6N), which

match well with the drop test (as shown in Figure 9. The 1.8m (6ft) drop test (Figure 9 - right) shows significant separation between the sum of the load cells and the total measured load. This deviation is likely due to the hysteresis among the individual load cells and propagation of errors acquired during bias calibration at load cell startup. In a static environment the two total parachute load estimates correlate; however, during dynamic motion the stretch in the nylon suspension lines appears to maintain minor loads even when unloaded (recall the load cells exhibit 8% hysteresis on average). Further validation of the hysteresis hypothesis comes from the excellent correlation of total load estimates prior to inflation, with deviations occurring during/immediately after snatch loading occurs.

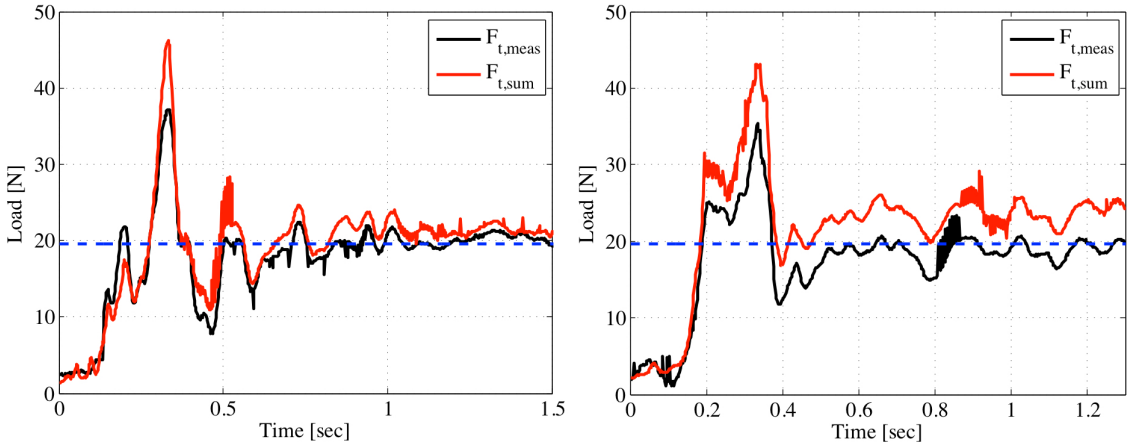

Figure 9: Comparison between sum of individual line loads with measured total load for a 0m (left) and 1.8m (right) static line drop test.

Another aspect examined in pursuit of validating the load distribution measurement system focused on comparing the terminal velocity and inflation times of the two

configurations tested. The estimated terminal velocity and total load measurement results can be seen in Table 2. The terminal velocity average for was 5.83 m/s and 6.92 m/s for the 0m and 1.8m (6ft) static line lengths, respectively. As expected, the 1.8m (6ft) static line exhibited a greater terminal velocity because the drop height does not provide sufficient time for the canopy to reach terminal velocity before reaching the ground. The 0m static line drop tests had lower velocities at inflation, providing sufficient time for the canopy-payload to reach terminal velocity prior to impacting the ground. The 0m static line drop tests had an average inflation time of 0.40s. The longer static line drop tests had higher inflation velocities, resulting in a shorter average inflation time of 0.26s. Although there are some small deviations between total loads, the measurement system does provide an accurate measurement of total load; therefore, each individual load cell is also accurately measuring the suspension line loads.

Table 2: Summary of Drop Testing Results With Suspension line Load Cells

Static Line (m)	**Terminal Velocity** (m/s)	**Time to Inflation** (s)	**Peak Load** $F_{t,sum}$ (N)	**Peak Load** $F_{t,meas}$ (N)
0	5.46	0.33	46.1	37.2
0	5.98	0.47	41.5	36.7
0	6.06	0.41	54.1	49.2
1.8	6.29	0.23	43.1	35.4
1.8	7.17	0.31	50.4	44.6
1.8	7.31	0.24	50.1	41.6

3.3.2 Load Asymmetry Results

Using the validated custom suspension line load cells, the analysis of canopy asymmetry during inflation and terminal descent was conducted. Representative asymmetry results at peak load from a single drop test with a payload mass of 2kg (4.4lbs) and 0m length static line deployment are shown in Figure 10. As shown, LC_1 is over 25% larger than the average load at peak load. The observed asymmetry corroborates well with the Orion parachute investigation, which provided similar asymmetric loading patterns on full-scale parachute systems.

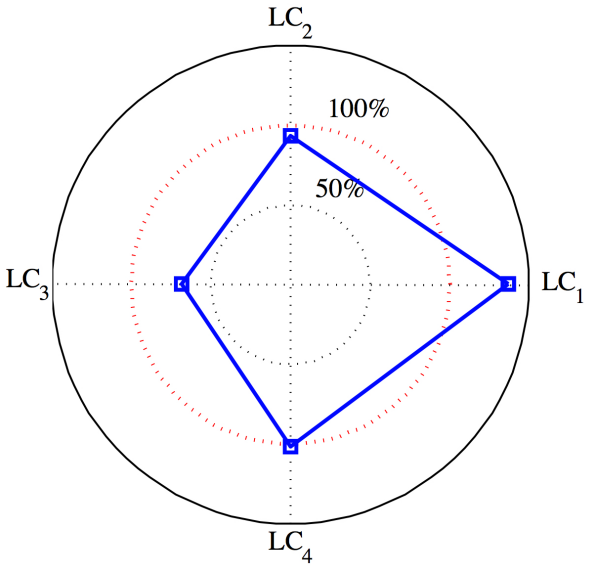

Figure 10: Parachute load distribution at peak loading during drop testing.

Knacke's Parachute Recovery Systems Design Manual recommends an asymmetric loading factor of 1.1 for calculating a parachute design factor; however no method for calculating the asymmetric loading factor is given. For this study, the point-by-point

asymmetric loading factor, s_i, is calculated from the maximum loading factor (maximum determined from the four suspension line load cells) at for each time step.

$$s_i = max(\frac{LC_{1,i}}{LC_{avg,i}}, \frac{LC_{2,i}}{LC_{avg,i}}, \frac{LC_{3,i}}{LC_{avg,i}}, \frac{LC_{4,i}}{LC_{avg,i}}) \tag{3.2}$$

An overall maximum asymmetric loading factor, s_{max}, and average asymmetric loading factor, s_{avg}, can then be quantified from the point-by-point asymmetric loading factor calculations. As shown in Table 3, significant asymmetric loading results were observed in all drop tests, yielding an asymmetric loading factor (both maximum and average) always greater than 1.1. The 0m static line length resulted in a maximum asymmetric factor of 2.13 which indicates at the time of max asymmetry one of the suspension lines experienced more than twice the average load of the four load cells. The average asymmetric loading factor for the 0m static line was 1.25, demonstrating a 15% increase from the traditional 1.1 asymmetric loading factor. The 1.8m (6ft) static line length drop tests resulted in a maximum asymmetric loading factor of 1.8; significantly less than the 0m static line. This is to be expected as the suspension lines were released at a high rate of speed at the same time, producing a more uniform suspension line snatch load (as the 0m static line initiates inflation from rest). The 1.8m (6ft) static line results show an overall drop test asymmetric average factor of 1.18; which is also greater than the traditional recommended design of 1.1. It is important to note that the two average asymmetric loading factors of 1.25 and 1.18, are averages over an *entire* drop test. For design purposes, the maximum asymmetric loading factor should be used to ensure the suspension lines

are capable of handling the larger loads. Figure 10 shows asymmetry during peak inflation, however the maximum asymmetrical load typically occurs between peak load and immediately following the inflation event. The results indicate substantially larger asymmetry loads than previously accounted for in parachute design. For maximum safety and parachute system vehicle robustness, a larger asymmetric load factor should be incorporated into the parachute design phase.

Table 3: Asymmetric Load Factors

Static Line	**Drop #1**		**Drop #2**		**Drop #3**	
(m)	s_{avg}	s_{max}	s_{avg}	s_{max}	s_{avg}	s_{max}
0	1.25	1.98	1.25	2.00	1.23	2.13
1.83	1.18	1.66	1.13	1.67	1.18	1.80

3.3.3 Load Cell Dynamics Effect

To fully investigate the load distribution measurement system, flight testing was conducted to identify the effects of the suspension line load cells on the overall parachute behavior. This was accomplished by performing all drop testing both with and without suspension line load cells. Data was compared from the total load measuring load cell, $F_{t,meas}$, between the various drop tests experiments.

Figure 11 shows representative drop test data of the total measured force of two separate drop tests with a 0m static line. One drop performed with all suspension line load cells, and the other was performed without any suspension line load cells. The peak load

with load cells attached is 37.23N and the peak load without load cells is 37.16N demonstrating less than 0.08N difference in peak loads for a single drop test performed in identical testing conditions. The steady state load of 19.61N for a 2kg (4.4lbs) payload weight is also achieved to further validate that the suspension line measurement system has a negligible effect (at least within the accuracies achieved in this study) on the parachute flight dynamics. The loading time series also lines up well with cross-correlation data showing high-confidence in matching loading results for all flight tests. The barometric pressure transducer housed in the payload was used to estimate the terminal velocity, but could not be used to estimate the velocity at peak inflation. The pressure transducer has a maximum sampling rate of 10 Hz, and the inflation occurs within the first 0.1-0.2 seconds after release.

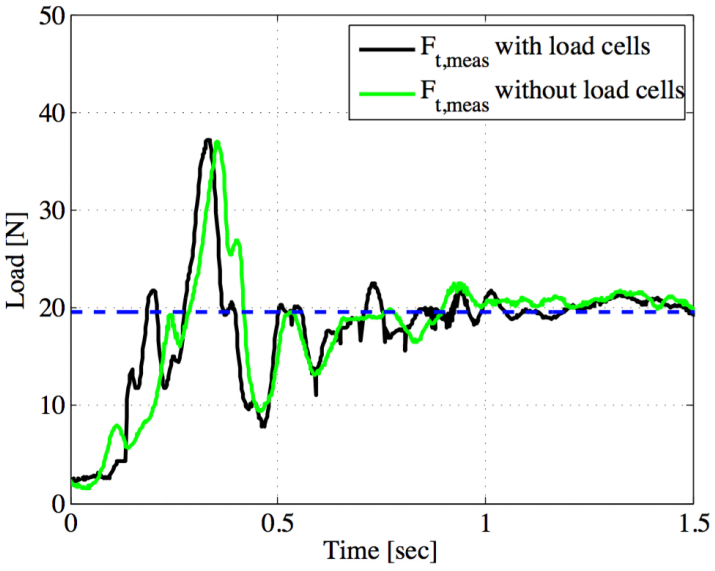

Figure 11: Comparison between a drop with suspension line load cells and a drop without suspension line load cells.

Table 4 shows the terminal velocity, time to inflation, and measured peak load. For the 0m static line, the *difference* between drop tests with and without load cells average terminal velocity, time to inflation, and total load was 0.13m/s, 0.07s, and 0.7N, respectively. The 1.8m (6ft) static line drop tests showed a *difference* between testing with and without load cells for the terminal velocity, time to inflation, and total load of 0.04m/s, 0.01s, and 0.3N, respectively. The differences for both drop scenarios produced very small deviations between testing with and without the attached custom load cells. Many of the deviations are within the measurement uncertainty of the developed system; therefore, it can be concluded that even on the small-scale parachute used in testing, the non-invasive load cells did not have a significant effect on the parachute behavior. For larger parachute systems, the increased weight from load cell redesign (thicker cantilever section) will be minimal, compared to the increase in parachute-payload size.

Table 4: Average Results With and Without Suspension Line load Cells Comparison

Static Line	**Suspension Line Load Cells**	**Terminal Velocity** (m/s)	**Time to Inflation** (s)	**Peak Load** (N)
0m	With	6.92	0.26	40.5
	Without	6.79	0.19	39.8
1.8m	With	5.83	0.40	37.0
	Without	5.87	0.39	36.7

3.4 Conclusion

A wireless parachute load distribution measurement system was designed, calibrated, validated, and drop tested. A redesigned signal conditioner was coupled with the

previously developed load cell design, which provided the capability to perform bias corrections via software, greatly enhancing the measurement systems robustness. Parachute load measurement validation was conducted with both a static calibration as well as with in-flight measurements of individual suspension lines and compared with total parachute load. Drop testing was conducted with a guide-line drop rig with a servo actuated release mechanism at 0m and 1.8m (6ft) static line lengths and a 2.0kg (4.4lbs) payload weight.

Results demonstrated the capability of the load distribution measurement system to measure the total load and asymmetric loading during inflation and terminal descent. Results obtained from the validation phase of this work show the total load estimated from the sum of the individual load cells was within an average of 0.7N of the payload weight (measured during terminal descent). The sum of the individual load cells($LC_1 - LC_4$) also matches with the load cell mounted below the suspension line confluence point(LC_T) during most flight tests. Using the validated load cell measurement system, drop testing was performed to quantify the load asymmetry during inflation. Results showed a significant variation in suspension line loading during inflation, with maximum asymmetric loading factors exceeding twice the average suspension line load (greatly exceeding the standard asymmetric loading factor of 1.1 used for current parachute design). Additionally, the average asymmetric loading factor exceeded the traditional asymmetric factor, demonstrating the highly dynamic motion of parachutes in controlled conditions. Descent velocity estimates obtained from a barometric pressure transducer were used in conjunction with total load measurements and inflation time to quantify the effects of the load cells on

parachute flight dynamics. Results concluded that the individual load cells had a negligible effect on parachute flight dynamics even for the small-scale parachute system used in this study. The system presented in pursuit of the first objective has been met with the conclusion above. The circular parachute load measurement system was developed and tested.

CHAPTER 4

FEASIBILITY OF IN-FLIGHT QUADROTOR INDIVIDUAL MOTOR THRUST MEASUREMENTS

This information can be found in the conference proceedings of the 2016 AIAA Science and Technology Forum and Exposition, San Diego, California

4.1 Introduction

Unmanned aircraft have seen tremendous growth over the past two decades for a wide range of applications including: surveillance, land surveying, and search and rescue [23,37,39]. Additionally, use of small unmanned aircraft for agricultural crop inspection and monitoring has demonstrated excellent benefits over traditional techniques [38]. However, unmanned systems currently have a significantly higher accident rate than their human-piloted counterparts. Based on an analysis of the more than 400 military drone accident reports, many of the unmanned aircraft accidents were due to mechanical defects [54]. For small unmanned aircraft systems (UAS) the accident rate is significantly higher (particularly among hobbyist/amateur pilots) due to the rapid development, limited testing of the various lightweight aircraft systems, and insufficient pilot training. Cases of small unmanned aircraft crashing into public areas have increased substantially over the past several years [48,49].

One aspect necessary for improving flight stability is the accurate estimation of the aircraft motor/engine thrust. For multirotor small unmanned aircraft, the motor thrusts are

typically estimated from either the motor command or the motor angular velocity [2]. Unfortunately, both thrust estimation techniques do not accurately describe the actual thrust force during all modes of flight [2] as the techniques are essentially feedforward control models. Particularly during in-flight anomalies (propeller failure, speed controller communication loss, excessive rotation rates, etc.), the actual thrust force can be substantially different from the estimated force without sensory feedback. The thrust forces an be measured through rigidly mounting the aircraft to a load cell; however, this provides only a calibration of the total vehicle thrust for a given motor command or motor angular velocity [26].

Another approach to estimate the thrust forces is with a load cell attached to each motor (or embedded into the cantilever beam as used in this study). However, without implementing a corrective algorithm it is not possible to isolate the individual motor thrust forces of a quadcopter during unconstrained flight. This is primarily due to the rotational and translational acceleration-based inertial forces modifying the measured thrust force. In this study the thrust forces are indirectly measured via a combination of motion capture-based state information coupled with a full-bridge strain gauge assembly mounted directly onto each of the four quadcopter arms. The strain gauge units provide the capability to measure the combined thrust force and the effective inertial force, thereby requiring the accurate knowledge of the vehicle states to resolve the individual thrust forces. For this study the thrust forces are estimated by post-processing flight test data; however, real-time estimates can be performed with many of the currently available microcontrollers.

Estimation of the actual thrust forces provides useful vehicle information for the

development of improved fault-tolerant control systems, thereby improving the robustness and safety of the aircraft. Current fault tolerant control techniques typically incorporate a range of pre-programmed control systems intended for a particular failure scenario [22, 41]. Fault identification is accomplished by examining the state information given the system inputs, and correlating anomalies to a preprogrammed failure scenario. Upon fault identification, the appropriate control system is used to maintain stability and improve survivability. Unfortunately, the fault tolerant control systems are specific to each individual vehicle, and only a discrete number of failures are pre-programmed (i.e. partial failures may not be included in the control system). The estimation of the individual motor thrust forces enables continuous feedback of the motor thrusts, providing the capability to implement continuous fault-tolerant control strategies.

4.2 Methodology

The development methodology for the motor thrust estimation system has been split into three sections. First, the model development section discusses the development of the thrust estimation algorithm that includes the inertial force compensation. Next, the physical aircraft used for testing is discussed with particular emphasis on the strain gauge sensors mounted to the aircraft. Finally, the four stages of testing and the associated evaluation metrics are described.

4.2.1 Model Development

Mounting strain gauges to each arm of the quadcopter provides quantification of the total force (inertial and thrust forces) at each motor location (as this is the calibration location for the strain gauges), but only the thrust forces are desired for use in flight controller development. The measured forces are the combination of the individual thrust forces and the effective inertial forces at each motor location caused by rotational and translational acceleration. Compensation for the inertial forces can be computed using the translational equations of motion generated at each of the four quadcopter motor locations. In this chapter, I have the following figures:

$$\begin{bmatrix} F_{thrust}^{M1} \\ F_{thrust}^{M2} \\ F_{thrust}^{M3} \\ F_{thrust}^{M4} \end{bmatrix} = \begin{bmatrix} F_{meas}^{M1} \\ F_{meas}^{M2} \\ F_{meas}^{M3} \\ F_{meas}^{M4} \end{bmatrix} - \begin{bmatrix} m_{eff}^{M1\,N} \vec{\mathbf{a}}^{M1} \\ m_{eff}^{M2\,N} \vec{\mathbf{a}}^{M2} \\ m_{eff}^{M3\,N} \vec{\mathbf{a}}^{M3} \\ m_{eff}^{M4\,N} \vec{\mathbf{a}}^{M4} \end{bmatrix} \cdot \hat{\mathbf{b}}_z \tag{4.1}$$

The effective mass of each quadcopter arm is calculated by measuring the mass and location of each component on the arm, and estimating the effective mass if all of the components were placed at the motor location. This is analogous to calculating an effective mass for a compound pendulum that enables modeling as a particle pendulum. Using rigid body kinematics, the acceleration of each motor location ($M_1 - M_4$) can be estimated with the rigid body quadcopter center of mass (denoted BC) state information. The quadcopter states can be derived from onboard estimates or through motion capture data. For this study, the rotational and translational positions are estimated from motion capture data, and the corresponding velocity and acceleration estimates are estimated through a finite divided difference numerical derivative approximation that was

then filtered with a high-pass Butterworth filter. The high-pass filter removes the drift thrust estimates associated with the inevitable strain gauge output drift. The translational acceleration of each motor can be calculated using the aircraft state information and the *a priori* known distance between each motor and the center of the aircraft ($\underset{\rightarrow}{\mathbf{r}}^{M1/BC}$).

$$ {}^{N}\underset{\rightarrow}{\mathbf{a}}^{M1} = {}^{N}\underset{\rightarrow}{\mathbf{a}}^{BC} + {}^{N}\underset{\rightarrow}{\boldsymbol{\alpha}}^{B} \times \underset{\rightarrow}{\mathbf{r}}^{M1/BC} + {}^{N}\underset{\rightarrow}{\boldsymbol{\omega}}^{B} \times \left({}^{N}\underset{\rightarrow}{\boldsymbol{\omega}}^{B} \times \underset{\rightarrow}{\mathbf{r}}^{M1/BC} \right) \tag{4.2} $$

The motion capture-based rotational velocity and acceleration estimates are in the traditional Euler frames; however, generalized speeds can be incorporated to transform the rotational velocity and acceleration estimates to the body-fixed axis, $\hat{\mathbf{b}}_{xyz}$. The generalized speeds are defined such that:

$$ {}^{N}\underset{\rightarrow}{\boldsymbol{\omega}}^{B} = U_1\hat{\mathbf{b}}_x + U_2\hat{\mathbf{b}}_y + U_3\hat{\mathbf{b}}_z \tag{4.3} $$

The kinematic equations can then be solved by simultaneously solving the three rotational equations for the motion capture rate/acceleration estimates. The translational generalized speeds are simply the derivative of the inertial positions. The kinematic relationships enable a more intuitive analysis of the data, particularly when examining the resulting motor location acceleration.

$$ \begin{bmatrix} \dot{q}_{rx} \\ \dot{q}_{ry} \\ \dot{q}_{rz} \\ \dot{q}_{tx} \\ \dot{q}_{ty} \\ \dot{q}_{tz} \end{bmatrix} = \begin{bmatrix} \frac{\cos q_{rz}U_1 - \sin q_{rz}U_2}{\cos q_{ry}} \\ \sin q_{rz}U_1 + \cos q_{rz}U_2 \\ U_3 + \tan q_{ry}\left(\sin q_{rz}U_2 - \cos q_{rz}U_1\right) \\ U_4 \\ U_5 \\ U_6 \end{bmatrix} \tag{4.4} $$

The resulting equations can then be used to transform measured forces to the estimated thrust forces for each of the four motors. It is important to note that the quality of the aircraft states will directly impact the quality of the estimated thrust forces.

4.2.2 Hardware

The quadcopter frame (Figure 12) developed for this study was created with flat aluminum bars and various off-the-shelf components. The base plates have a diameter of 0.16m (6.25in) and the aluminum arms extend from the base plates 0.27m (10.75in). The resulting quadcopter motor-to-motor diameter is 0.67m (26.50in). The brushless motors used were coupled with 0.23m (9.0in) propellers capable of producing a maximum thrust of 7.8N (1.76lb) (DJI Phantom 2312). Electronic speed control for the four motors was provided by DJI E310 speed controllers. Aircraft stabilization was controlled via flight controller in the "attitude" stabilization mode (DJI NAZA-m Lite). The easy-to-use flight controller features an all-in-one design containing inner damping, 3-axis gyroscope, 3-axis accelerometer, and a barometer housed in the unit. The inexpensive flight controller provides a robust system for safe multirotor flight operations, removing custom flight control safety and stability concerns and enabling a thorough investigation of the thrust measurement capabilities of the strain gauge system.

Thin film strain gauges (Omega) were placed on each quadcopter arm in a full Wheatstone bridge configuration (four gauges per arm). Each pair of gauges were fixed together by the manufacturer, reducing errors in alignment during sensor mounting. Each strain gauge has a 1000Ω resistance with a manufacturer provided gauge factor of 2.13.

Figure 12: Constructed quadcopter with instrumented arms mounted onto load cell test stand.

The full bridge configuration provides increased strain sensitivity while simultaneously compensating for axial loading and temperature-induced strain. The gauge locations were determined such that with an estimated loading (both thrust and inertial) of 17.8N (4.0 lb), the resulting strain at the gauges would be approximately $1,600\mu\epsilon$. The necessary strain gauge locations were calculated to be 24.1 cm (9.5 in) from the motor mounting locations.

The raw voltage from the strain gauges was acquired with a National Instruments (NI) 24 bit A/D strain module (NI 9237). The NI module was used for all calibration, load cell testing, oscillatory testing, and free flight testing. To mitigate errors associated with aliasing, samples were acquired at 2kHz for 10 seconds. The NI module was tethered to the aircraft with 3.7m (12 ft) of bundled data cable connected to each of the Wheatstone bridge circuits. It is important to note that all testing and calibration was performed with the tether in order to eliminate any errors associated with the tether resistance.

4.2.3 Testing Methodology

To evaluate the feasibility of the thrust measurement system, four different tests were conducted: 1) individual arm/load cell calibration, 2) static total thrust verification, 3) inertial force compensation evaluation, and 4) free flight testing with inertial force compensation evaluation. The four testing phases provide thrust measurement confidence levels in increasingly complex flight scenarios.

A static calibration of each quadcopter arm was performed during the first phase of evaluation of the strain gauge thrust measurement system. Each aluminum arm was fixed at the proper base mounting location with known weights applied at the motor mount location to simulate a static thrust. Each arm was calibrated in accordance to standard calibration procedures [1,5] with two trials performed for each individual arm with ascending and descending applied loads. The calibration procedure performed provides estimates of the Wheatstone bridge hysteresis, repeatability, and linearity in the quadcopter arm force measurements. Each arm was calibrated to a rated capacity of 15.7N (3.5 lb).

Once the individual arms were calibrated, the quadcopter was assembled and attached to a six degree-of-freedom load cell (Bertec PY6-50). The six-axis load cell directly measures all three forces and moments with $\pm 0.08N$ and $\pm 0.001N-m$ accuracies, respectively. For total thrust strain gauge evaluation, only the vertical axis of the load cell was used (rated capacity of 50 lb). The device has an internal 16-bit digital signal acquisition which permits interfacing directly with a computer through USB. To validate the total aircraft thrust measurement accuracy, the individual thrust forces were summed and compared to the six-axis load cell vertical load data. Achieving repeatable results

proved difficult with the NAZA flight controller because it produces a constantly varying motor command to maintain vehicle stability [26]. Therefore the NAZA was not used in the six-axis load cell verification tests. Identical commands were programmed using a microprocessor and sent directly to each electronic speed controller. The programmed signal consisted of a time varying triangle wave with five total cycles at three different frequencies. The first cycle had a period of 3.08s, cycles two and three had periods of 1.98s, and cycles four and five had periods of 0.88s. This test was performed to give an order of increasingly complex scenarios for the load cells to measure. The triangle wave allowed for a dynamic test of the system without having to test it in free flight. The data was collected at 500Hz for 10 seconds on the six-axis load cell and at 2000Hz for 10 seconds on the strain gauge load cells. The data was then interpolated to match the time series between the six-axis load reading and the strain gauge load reading. Time syncing between the strain measurement and the six-axis load cell was accomplished via cross-correlation between the two data sets. Cross-correlation was used to determine the phase lag between the signals. The phase lag allowed for adjustment from one signal to the other.

As mentioned previously, the measured arm forces do not directly represent the actual thrust forces of the quadcopter motors/propellers, because of the inertial forces acting on the quadcopter arms. To evaluate the performance of the inertial force compensation in as controlled an environment as possible, testing was performed in which the quadcopter motors were not in operation. The quadrotor was suspended by constraining two of the four arms. It was then rotated about the axis of the two constrained arms

(aircraft pitch direction) in an oscillatory motion manually. The manual rotation of the quadrotor was accomplished by imposing a moment at the base of the aircraft such that nearly all of the measured force was due to inertial components alone. An example of the quadcopter pitch motion rotated at 0.8 Hz is shown in Figure 13.

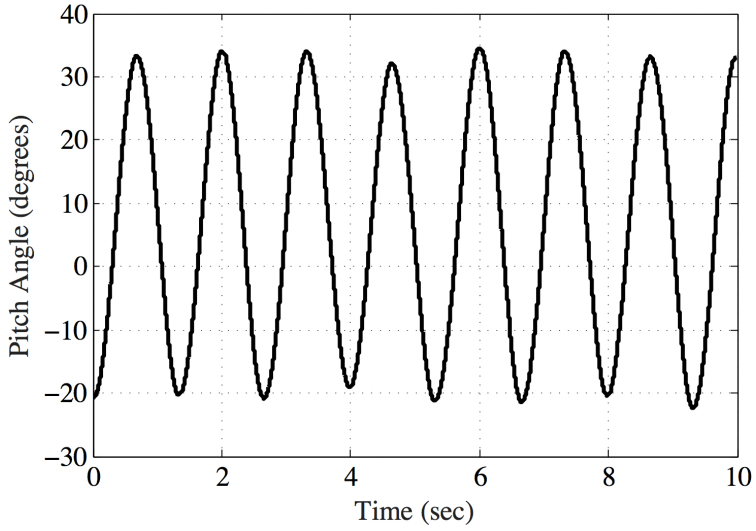

Figure 13: Pitch motion generated manually for testing at an oscillatory rate of 0.8 Hz

A metronome was used to improve oscillation frequency accuracy of the manual rotation motion. A Fast Fourier Transform (FFT) was performed on the data to identify the actual oscillation frequency for each trial. Due to the human-provided initial conditions, the repeatability of the experiments can only be approximated; however, the metronome aided tremendously in reducing frequency variability. As mentioned previously, motion capture was used to estimate rotational state information. All flight test data was processed offline after data alignment between the two sources. The motion capture records

data at a rate of 100 Hz and the strain gauge load cells record data at a rate of 2000 Hz. Interpolation between the motion capture and strain data was performed post process before time syncing each trial. Time syncing between motion capture data and measured strain data from the quadrotor was accomplished via cross-correlation in the same procedure that was as performed for the load cell validation.

The root mean squared error (RMSE) metric was used to quantify the thrust estimation capabilities for all testing scenarios. Two fundamentally different RMSE quantities were used in this study. For both fixed-vehicle total thrust evaluation and motor-free inertial force compensation evaluation the RMSE could be computed between the estimated thrust force and the known thrust force. In these scenarios the RMSE reflects the proximity of the thrust estimation technique with a reference. For the free-flight testing it is impossible to have a known thrust force, as the vehicle is in motion constantly. During free-flight testing, the RMSE is used to compare the estimated thrust force and the measured arm force (directly from the strain gauge sensor). This metric provides quantification of the necessity to compensate the raw force measurement with the acceleration quantities discussed previously. If the RMSE is near zero, then there is little to no compensation required for the particular maneuver being examined. Conversely, if the RMSE is not zero, then the compensation *may* be providing more accurate results. It is important to note that in free-flight the true force is not known, and therefore, the thrust estimates may not be closer to the true values. This is why the testing evaluation was conducted in so many stages, as if each testing stage demonstrates success, then it is likely that the complete thrust estimate algorithm is providing accurate results.

$$RMSE = \sqrt{\frac{1}{N}\sum_{i=1}^{N}(s_{meas} - s_{true})^2} \tag{4.5}$$

Free flight testing was conducted after evaluation of the thrust measurement system's capabilities in both static thrust and inertial force compensation. During the described indoor flight testing operations position and rotation information was acquired from a motion capture system (OptiTrack Flex 13 cameras) in a 6.1m x 6.1m x 3.1m (20ft x 20ft x 10ft) flight volume at a rate of 100 Hz. Time syncing between the onboard strain measurement and the motion capture data was accomplished via cross-correlation between the measured force data and the estimated force data from Eq. 4.1 using the same procedure described for the strain gauge system validation. Two flight scenarios were investigated including pitch motion and yaw motion. The flight conditions provide thrust forces such that the inertial forces are near zero, constant, or time varying.

Each experiment provides valuable insight into the estimated motor thrust forces, and provides a useful information for both dynamic modeling and actuator feedback necessary for improved flight control. However; the true thrust force is still only estimated and not known with certainty. These tests results will provide an intuitive understanding of what certain maneuvers will do to the force, without knowing it's true value.

4.3 Results and Discussion

4.3.1 Individual Arm Calibration

Each quadcopter arm, with installed strain gauges, was mounted to the bench top for individual arm calibration. Nylon string was attached directly below the center of

the motor to simulate loading applied as closely to the center of the motor as possible. Strain data was collected in LabVIEW with the NI 9237 input module at a rate of 2kHz. Known weights of 0g, 100g (0.22 lb), 600g (1.3 lb), 1100g (2.4 lb), and 1600g (3.5 lb) were applied in ascending and descending orders twice to give measures of hysteresis, repeatability, and linearity. A representative strain gauge calibration plot is shown in Figure 14. The single arm load cell has excellent hysteresis error (0.08% of rated capacity), repeatability error (0.12% of rated capacity), and linearity error (0.12% of rated capacity). The estimated custom load cell characteristics are similar to the characteristics of traditional off-the-shelf load cell products. It is important to note that for this study off axis loading errors were not investigated; however, the shape of the quadcopter arms provides excellent rigidity in all but vertical bending and torsion directions.

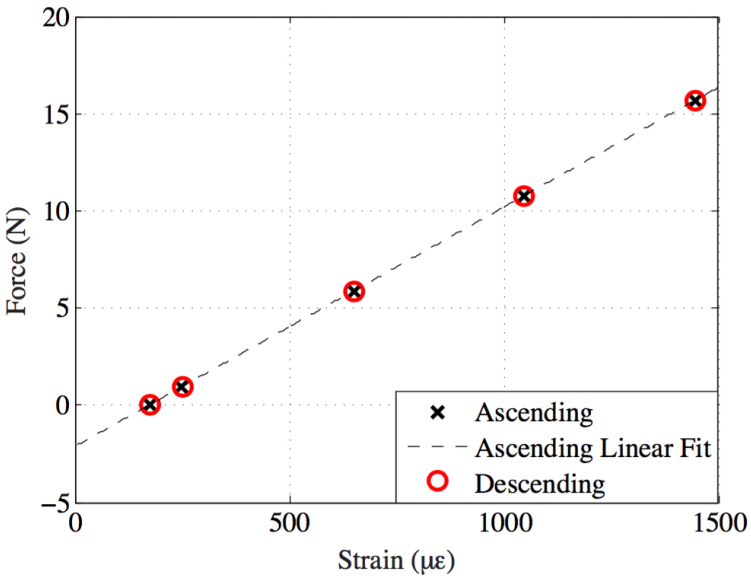

Figure 14: Calibration data from a single quadcopter arm with both ascending and descending arm loading.

4.3.2 Total Thrust Measurement Testing

Upon completion of individual arm strain gauge calibrations, the quadcopter was fully assembled and attached to the six-axis load cell for total thrust measurement verification. Identical to the calibration phase of testing, the strain gauge data was acquired from all four quadcopter arms via LabVIEW at a rate of 2kHz. As mentioned previously, the motors were given preprogrammed commands to provide repeatability in the measurements. The programmed motor routine was performed four times, with a representative time history of both the summed arm load cells and the directly measured total load is shown in Figure 15. The Pearson correlation coefficient between the summed thrust forces and the directly measured total load was calculated to be 0.99, indicating a strong correlation between the two total force estimates. The primary difference between the two thrust estimates occurs during peak thrust at all oscillation frequencies used. The exact cause of the discrepancy is unknown; however, it is theorized that the difference may be due to a portion of the total thrust force is not in the vertical direction (in the six-axis load cell's x and y axis) or caused by hysteresis effects not identified during the static calibration.

The root mean squared error (RMSE) between the summed thrust forces and the directly measured total load for one of the four experimental runs was 4.53N (1.0 lb). As a baseline for comparison of the RMSE, the RMSE between two summed thrust forces from two different experimental runs was 1.73N (0.39 lb). Therefore, the difference between the directly and summed total thrust force measurements is approximately double the RMSE between the same measurement of two experimental trials. The results indicate

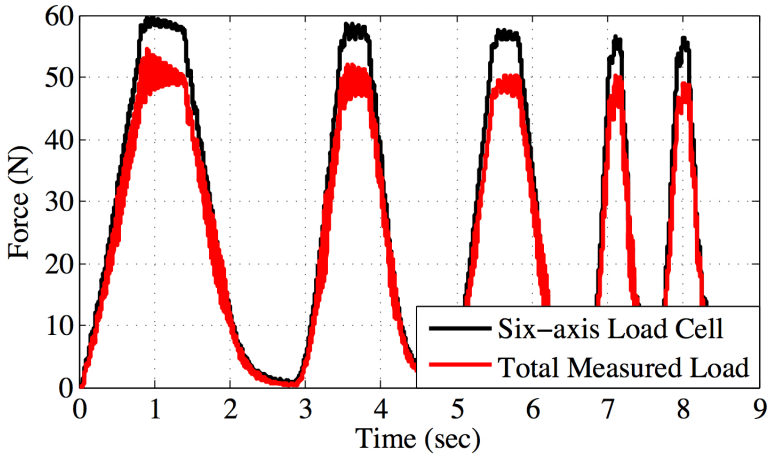

Figure 15: Total estimated load with the four strain gauge-based load cells compared with the measured resultant thrust with prescribed transient input commands.

exceptional force estimation for all but the maximum thrust forces (greater than $50N$), which are rarely experienced during nominal flight conditions.

Table 5: RMSE values for all total thrust measurement trials

Trial	**RMSE**
1	4.79N
2	4.57N
3	4.60N
4	4.53N

4.3.3 Inertial Force Compensation

Prior to conducting the pendulum-style testing, a free-flight test was conducted to determine the dominant frequency of the quadrotor motion during nominal flight. A Fast Fourier Transform (FFT) was performed on the data from the free-flight test and is shown in Figure 16. A yaw motion and a pitch motion were performed during the flight test and

the dominant frequency of the overall motion was found to be 0.4 Hz. The FFT shows that the dominant frequency range is from 0.1 to 2.0 Hz. Therefore, to evaluate the motion effects on the thrust measurements during free-flight, the range of excitation frequencies can be limited to within 0.1 and 2.0 Hz during pendulum-style testing.

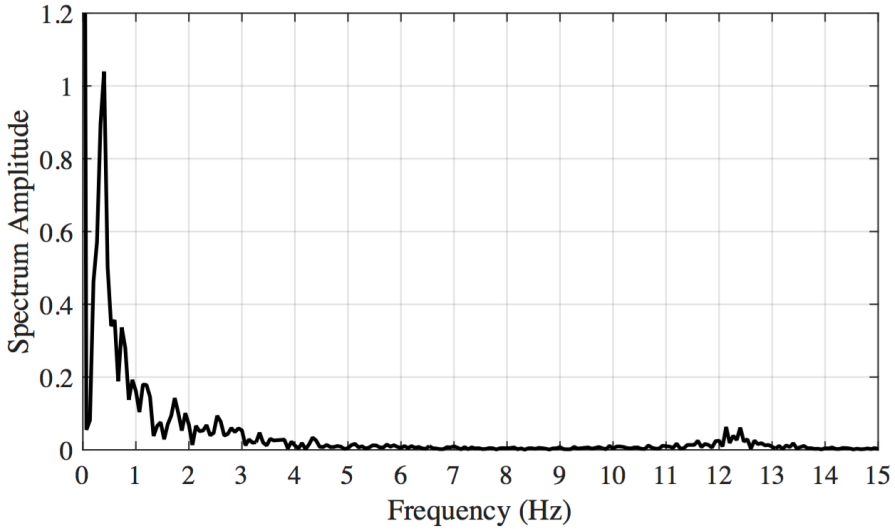

Figure 16: FFT from free flight maneuvers showing dominant frequency of quadrotor movement.

Once the dominant frequency range was found using the FFT, a series of oscillatory rotation tests were performed at varying frequencies within the determined range. The quadrotor was suspended by two arms and rotated manually about the Y axis (pitching motion) in a pendulum motion at seven different frequencies. A metronome was used to give the user a physical representation of the frequency to manually rotate the quadrotor. This series of tests were performed without motor power to determine the influence of inertial forces on the thrust measurements and evaluate the inertial force compensation

capabilities of the thrust estimation algorithm. The measured thrust force and the corresponding estimated thrust force from inertial compensation for one of the quadcopter arms are shown in Figure 17 and Figure 18 for oscillation frequencies of 0.5 Hz and 0.9 Hz, respectively.

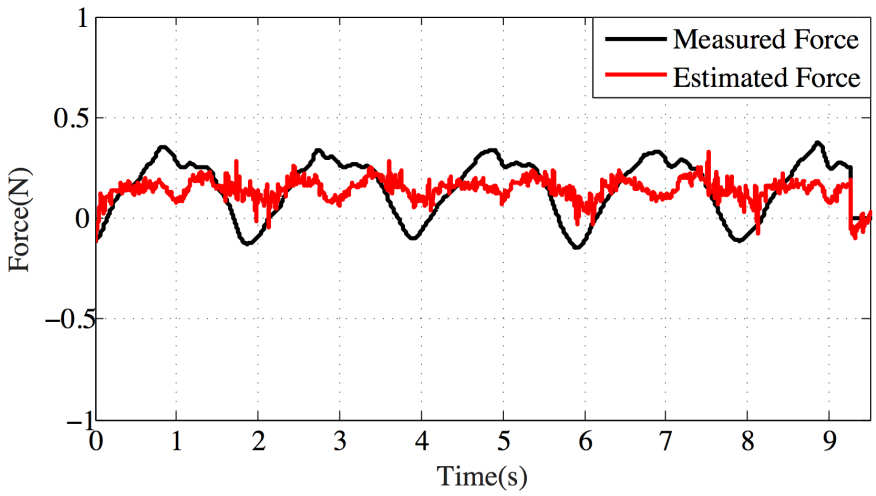

Figure 17: Motor-free rotation force estimates with a oscillatory period of 0.5 Hz

Two oscillation trials were performed at each frequency. The RMSE values were calculated from the measured and estimated forces of the two oscillating motors and compared to the true, zero thrust force value. The average RMSE was calculated for the measured RMSE and the estimated RMSE from the two motors for each trial (four RMSE values averaged for each frequency). The average RMSE quantities are shown in Figure 19 for the seven frequencies investigated. The error bars for each RMSE value was calculated from the standard deviation of the RMSE.

The RMSE data and the representative figures indicate that at low oscillation frequencies the thrust estimation algorithm can not confidently remove the inertial effects.

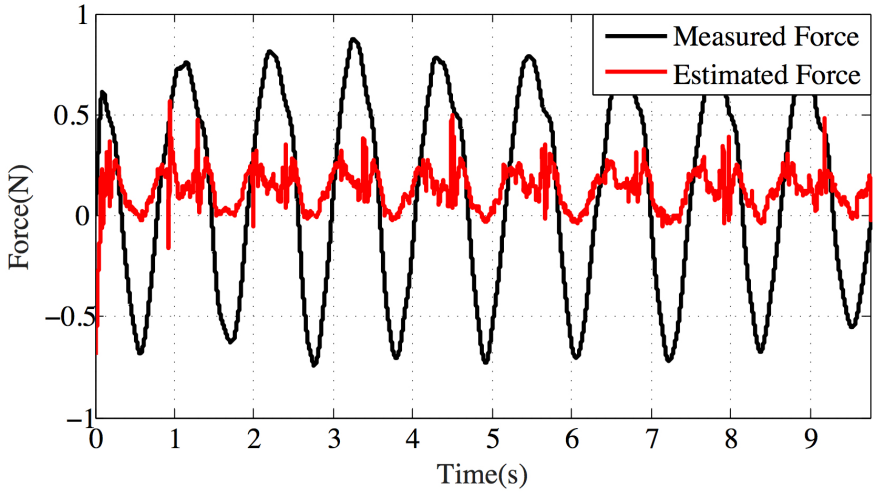

Figure 18: Motor-free rotation force estimates with a oscillatory period of 0.9 Hz

However, at higher oscillation frequencies the algorithm clearly reduces errors associated with using the measured force as a thrust force. High frequency maneuvers may occur during acrobatics, obstacle avoidance procedures, or during an in-flight failure event. During any of these scenarios, the current thrust estimation algorithm would provide significantly better estimates of the true motor thrust forces over estimates from the measured force or motor input command techniques. The reason for the lack of compensation at low frequencies can be attributed to the noisy state information coupled with performing two numerical derivatives of the state data. Using onboard state information from an inertial measurement unit would improve the signal to noise ratio of the inertial force estimates, thereby improving the compensation accuracy.

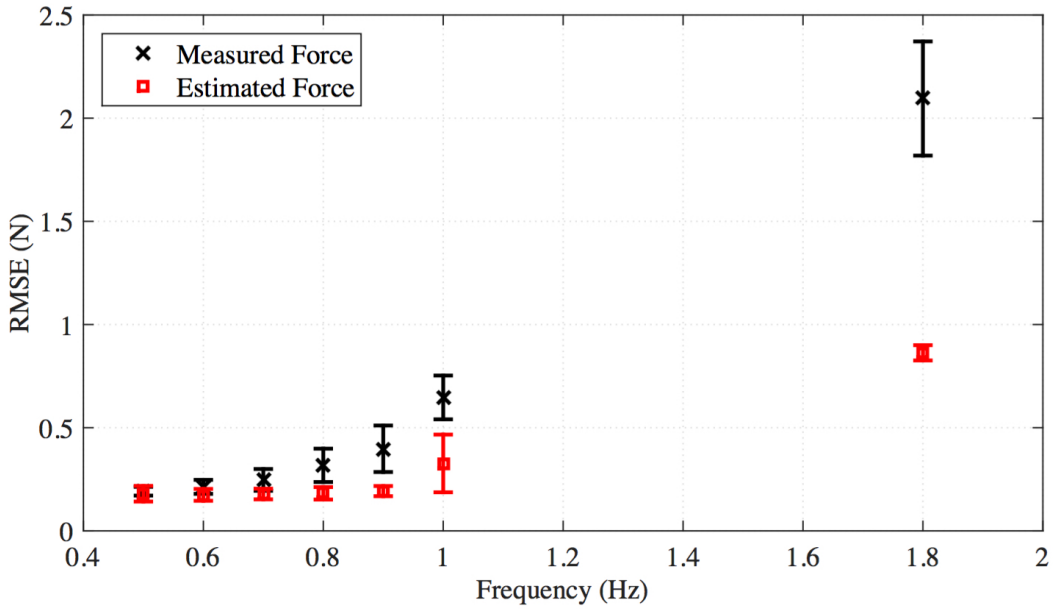

Figure 19: Average RMSE values for all Pendulum Frequencies

4.3.4 Free Flight Testing

A single free-flight test was performed to evaluate the effectiveness of the thrust estimation system. A representative thrust force (from a single motor) estimate from a yaw maneuver followed by a pitch maneuver is shown in Figure 20. Qualitatively the the measured thrust force from the yaw maneuver appears to be identical to the estimated thrust force with a simultaneous increase followed by a simultaneous decrease in the thrust force. The RMSE between the measured and estimated thrust force for the yaw phase of the flight (0-8.5 seconds) was 0.16N (0.036lb). The small RMSE value further indicates the minimal amount of compensation during a yaw maneuver. The high correlation between the two estimates follows intuition when considering how the aircraft yaws. Half of the motor speeds are increased, while the other two motor speeds are decreased, resulting in a non-zero aerodynamic torque applied to the aircraft. None of the acceleration

components are in the body-fixed z-axis during yaw, requiring no compensation from the estimation algorithm.

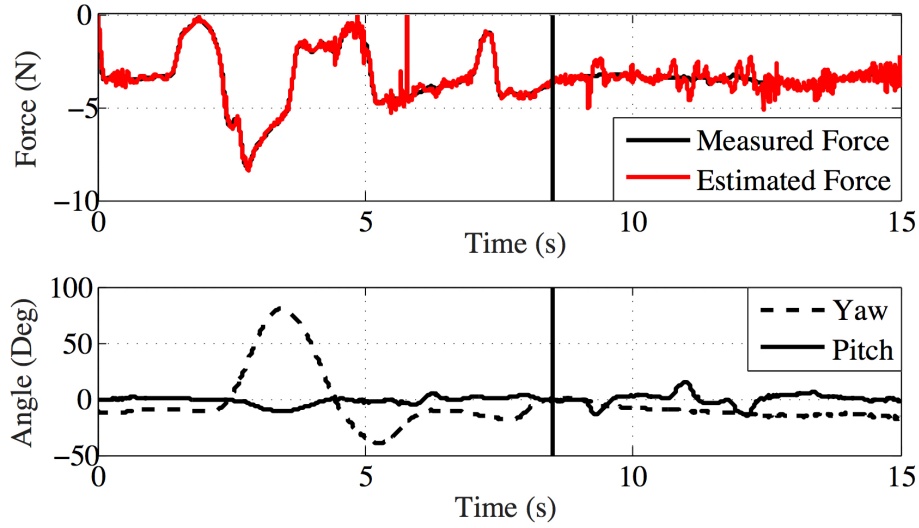

Figure 20: Measured force from motor one compared to the estimated force from motor one during a yaw and pitch maneuver in free-flight.

In contrast to the yaw maneuver, the pitch maneuver shows deviation between the measured and estimated thrust forces even with the relatively small pitch angles achieved during testing. The RMSE between the measured and estimated thrust force during the pitch phase of the flight test (8.5-15 seconds) was 0.34N (0.076lb). Although the true thrust forces are not known, the estimated thrust force does follow reasonable trends with the pitching motion. Typically, pitching motion occurs much faster than yawing motion, and can require inertial compensation. Additionally, the estimated thrust force does appear to oscillate about the measured force, indicating the measured thrust force may supply an average thrust force, while the estimated thrust force captures the higher frequency changes of the aircraft motors.

Without the ability to know the true motor force it is impossible to determine which of the two force estimates are closer to the true value. However, the inertial compensation algorithm does appear to track high frequency motion of the aircraft. This may render the estimation routine not useful for nominal flight conditions, but may be a significantly faster motor thrust estimation tool during aggressive motion of the aircraft. One example of the potential utility of the algorithm is during in-flight failure of a motor, ranging from partial failure to complete motor loss. The semi-direct measurement approach may provide faster feedback of the vehicle state, increasing the time for the flight controller to modify the control strategy to attempt to maintain flight stability.

4.4 Conclusion

The development and evaluation of an individual motor thrust estimation system has been described. A custom quadrotor frame was designed with embedded strain gauges installed directly on the arms for thrust measurement. The system was then calibrated, verified, and tested via indoor free-flight with the use of a motion capture system. The strain gauges-based force measurement sensors demonstrated comparable accuracy in measuring the forces acting at the motor mounting location when compared with current off-the-shelf load cell products. Using motion capture coupled with strain gauge data, a dynamic model was created to calculate the estimated thrust forces and compensate for any inertial forces caused by rotational and translational acceleration. The inertial force compensation was evaluated via free flight and static testing to show feasibility of the

proposed system. The thrust estimation system performs well at higher oscillation frequencies, but due to noise in the state data the estimation algorithm does not effectively negate inertial effects at lower oscillation frequencies. The estimation algorithm has significant potential for use in aggressive maneuvers, such as those experienced during in-flight failure potentially improving current fault-tolerant control strategies by reducing the fault-detection time during failure. The second objective of this thesis has been met with the conclusion above and with the development and evaluation of the strain gauge-based thrust estimation system.

CHAPTER 5

A COMPARATIVE STUDY BETWEEN REAL-TIME PARAMETER ESTIMATION AND STRAIN GAUGE-BASED ESTIMATION FOR QUADCOPTER ROTOR FAILURE DETECTION

This information can be found in the conference proceedings for the 2016 AIAA Region V Student Conference, Ames, Iowa

5.1 Introduction

Small unmanned aerial vehicles (UAV) have seen tremendous growth in population over the past decade. Small UAVs continue to be used for new and innovative applications such as search and rescue, land surveying, and crop inspection [23, 37, 39]. The versatility of small UAV is undeniable, as they can maneuver into precise locations and achieve feats previously unattainable with large aircraft. The most popular uses of small UAVs have stemmed from the ability to carry high resolution cameras. Small UAVs have even expended in Hollywood, enabling beautiful trailing camera angles that would have been unattainable without the ability of heavy lift multirotor UAVs [24]. Small UAVs are even being used by hobbyists in organized races for recreation purposes [11]. As the popularity and range of applications for small UAVs increases, the number of small UAV accidents will also increase. Some accidents can be attributed to pilot error, as many hobbyists do not have the proper/adequate training to fly the aircraft prior to conducting flight operations. However, many accidents can be attributed to a hardware failure (broken

propeller) or a software failure (defective/erratic flight controller). Flight controller technology has grown in conjunction with the popularity increase of small multirotor UAVs, but there is exists a need to develop new, robust control strategies. One of the most important aspects of robust flight development in small multirotor UAVs is the ability to detect and compensate for in-flight motor/propeller failures.

Real-time detection of a motor failure is an important and necessary component of a robust flight controller for multirotor aircraft. An obstacle of performing real-time fault detection is developing a technique that can be insensitive to noise, but still quickly detect a failure in the system [32]. Current fault tolerant control strategies involve pre-programed controllers designed for failures that are activated when a failure is detected [6]. Pre-programmed fault tolerant controllers are still required to compensate for time delays when attempting to detect a failure in order to implement the new control strategy [6]. Some methods combine different schemes of nonlinear state observers for fault detection as well [3, 56]. The work presented herein compares two real-time parameter estimation techniques in an effort to identify an effective real-time fault detection system for multirotor motor failures.

The first technique studied is a real-time parameter estimation in the frequency domain that uses equation error estimation coupled with a recursive Fourier transform. A benefit of the recursive Fourier transform technique is that the frequency domain automatically filters unwanted data, which significantly reduces computation time. The second technique studied is unique in-flight strain gauge-based thrust estimation system. Direct measurement of the individual motor thrust forces during free flight is not possible

due to inertial forces/moments acting on the quadcopter caused by rotational and translational acceleration. Typical thrust measurement systems require the vehicle to be rigidly mounted to a load cell, limiting thrust quantification to total thrust in a static flight rather than the thrust produced by individual motors during free flight [26]. The unique system used herein indirectly measures the thrust forces via on board state estimation coupled with full-bridge strain gauge assemblies incorporated directly into each of the four quadcopter arms. The strain gauges sensors measure the combined thrust force and the effective inertial force, requiring vehicle state knowledge to calculate the motor thrust forces. The unique strain gauge based measurement system demonstrated feasibility in a recent study [7], however the quality of the system has not been studied against a proven method of thrust estimation. Real-time parameter estimation in the frequency domain has been validated and verified as a reasonable approach to performing in-flight estimations [32].

5.2 Methodology

5.2.1 Hardware

The quadcopter frame (Figure 12) developed for this study has been custom made with instrumentation and cost in mind, utilizing inexpensive materials and off-the-shelf components wherever possible. There are two base plates that each have a diameter of 0.16m (6.25in)and four aluminum arms that extend outward 0.27m (10.75in) from between the plates. The resulting quadcopter motor-to-motor diameter is 0.67m (26.50in). The motors used were DJI Phantom 2312s coupled with 0.23m (9.0in) plastic propellers capable of producing a maximum thrust of 7.8N (1.76lb.). Electronic speed control for

the four motors was provided by DJI E310 speed controllers. Flight stabilization was required for free-flight testing and was achieved using the X-Monkey Cortex Navigation Platform (Ryan Mechatronics, USA). The stabilization came from a standard nonlinear dynamic inversion flight controller.

The X-Monkey was also used to record and store rotation and thrust data. The X-Monkey platform contains an ARM Cortex processor, GPS, six servo outputs, rate gyro, accelerometer, magnetometer, barometric pressure transducer, microSD card logging, two user serial ports, and several GPIO pins. Programming is performed in C, where the program framework was created to acquire sensor data, perform attitude estimations, and stabilize the aircraft. State estimates and measured strain gauge-acquired loads are recorded at 100 Hz. The raw voltage from the strain gauges was acquired with a Wheastone amplifier (RB-Onl-38) module originally designed for the Arduino. The module was adapted to be used with the X-Monkey analog input pins such that all data could be recorded on-board during flight series.

Thin film strain gauges (Omega, USA) were placed on each quadcopter arm in a full Wheatstone bridge configuration. A total of sixteen strain gauges were mounted (four on each arm) to the quadrotor. Each pair of gauges were fixed together by the manufacturer, which reduced potential alignment errors during installation. Each strain gauge has a 1000Ω resistance and a gauge factor of 2.13. The full bridge configuration provides increased strain sensitivity while simultaneously compensating for any temperature or axial load-induced strain. The gauge locations were determined through simple analysis such that with an estimated loading (both thrust and inertial) of 17.8N (4.0 lb.), the resulting

strain at the gauges would be approximately $1,600\mu\epsilon$. The resulting strain gauge locations were fixed at 24.1 cm (9.5 in) from the motor locations.

5.2.2 Strain Gauge Model Development

The full derivation of the strain gauge-based model is also in 4.2.1. The method is being redefined in this section for further clarification. For an individual quadcopter arm, two strain gauges were mounted on top, and two on the bottom. Each arm was capable of measuring only the bending load perpendicular to the quadrotor arms. The bending force can then be related to the thrust force in the individual arms from Equation 5.1.

$$\begin{bmatrix} F_{thrust}^{M1} \\ F_{thrust}^{M2} \\ F_{thrust}^{M3} \\ F_{thrust}^{M4} \end{bmatrix} = \begin{bmatrix} F_{meas}^{M1} \\ F_{meas}^{M2} \\ F_{meas}^{M3} \\ F_{meas}^{M4} \end{bmatrix} - \begin{bmatrix} m_{eff}^{M1\,N} \vec{\mathbf{a}}^{M1} \\ m_{eff}^{M2\,N} \vec{\mathbf{a}}^{M2} \\ m_{eff}^{M3\,N} \vec{\mathbf{a}}^{M3} \\ m_{eff}^{M4\,N} \vec{\mathbf{a}}^{M4} \end{bmatrix} \cdot \hat{\mathbf{b}}_z \tag{5.1}$$

The estimated thrust force for an individual motor is equal to the difference between the measured force from the strain gauge and the inertial force caused by the translational and rotational motion of the vehicle. The effective mass of the motor was estimated by measuring the mass of all of the components on the arm and their respective locations in relation to the motor (Equation 5.2). The effective mass was calculated as if all of the components were placed at the motor location, similar to modeling a compound pendulum as a particle pendulum.

$$m_{eff} = \frac{I}{L^2} \tag{5.2}$$

The acceleration of the individual motor location is determined from quadrotor rotational and translational motion. The acceleration of the individual motor location can be calculated using rigid body kinematics and knowing the quadrotor center of mass (Denoted BC) state information. The quadrotor rotational state information is recorded on-board via rate gyro and inertial measurement unit (IMU). The angular acceleration is derived from the angular velocity value via finite divided difference numerical derivative approximation. This acceleration value is then filtered with a low-pass Butterworth filter, reducing high-frequency noise attributed to the motor induced vibrations on the strain gauge measurements. The acceleration of the motor locations can then be estimated through rigid body kinematics (Equation 5.3).

$$ {}^{N}\underset{\rightarrow}{\mathbf{a}}^{M1} = {}^{N}\underset{\rightarrow}{\mathbf{a}}^{BC} + {}^{N}\underset{\rightarrow}{\boldsymbol{\alpha}}^{B} \times \underset{\rightarrow}{\mathbf{r}}^{M1/BC} + {}^{N}\underset{\rightarrow}{\boldsymbol{\omega}}^{B} \times \left({}^{N}\underset{\rightarrow}{\boldsymbol{\omega}}^{B} \times \underset{\rightarrow}{\mathbf{r}}^{M1/BC}\right) \tag{5.3} $$

The rotational velocity and acceleration values obtained are both in the traditional Euler frame, meaning they are rotations in space without a specified frame of reference. Generalized speeds can be incorporated into the model to transform rotational velocity and acceleration values to the body-fixed axis, $\hat{\mathbf{b}}_{xyz}$ [7]. The generalized speeds are defined in Equation 5.4 as the angular velocity of the quadcopter (body B) in the X, Y, and Z directions.

$$ {}^{N}\underset{\rightarrow}{\boldsymbol{\omega}}^{B} = U_1\hat{\mathbf{b}}_x + U_2\hat{\mathbf{b}}_y + U_3\hat{\mathbf{b}}_z \tag{5.4} $$

The translational generalized speeds are simply the derivative of the inertial positions, also known as the trial set kinematic relationship [31]. The kinematic equations for the rotational acceleration are shown in the Equation 5.5.

$$\begin{bmatrix} \dot{q}_{rx} \\ \dot{q}_{ry} \\ \dot{q}_{rz} \\ \dot{q}_{tx} \\ \dot{q}_{ty} \\ \dot{q}_{tz} \end{bmatrix} = \begin{bmatrix} \frac{\cos q_{rz} U_1 - \sin q_{rz} U_2}{\cos q_{ry}} \\ \sin q_{rz} U_1 + \cos q_{rz} U_2 \\ U_3 + \tan q_{ry} \left(\sin q_{rz} U_2 - \cos q_{rz} U_1 \right) \\ U_4 \\ U_5 \\ U_6 \end{bmatrix} \tag{5.5}$$

The rotational and translational accelerations (shown in Equation 5.5) can be used to take the measured forces from the strain gauges and estimate the thrust forces from each motor. The individual motor thrust forces can be used to calculate a constant parameter in the system, in this case the parameter calculated is the motor torque constant, K_{SG}. The method of thrust estimation described in this section will allow for the estimated motor thrust value at each point in time, therefore the calculation of the motor torque constant K_{SG} will be a single value at each point in time, shown in Equation 5.6. Calculating K_{SG} using a set of points for a better estimation of the value is described in the next section using a least squares method.

$$K_{SG} = \frac{((F_{thrust}^{M1} - F_{thrust}^{M3}) * L)/I_x}{Roll_{CMD} * 2} \tag{5.6}$$

5.2.3 Least Squares Parameter Estimation

A method for estimating linear model parameters using an equation error formulation in the frequency domain with a Fourier transform regression (FTR) was developed at NASA Langley Research Center for real-time estimation of aerodynamic and stability control derivatives of aircraft [32]. The model is decoupled with individual regressor equations for each axis of motion (pitch,roll,yaw). The roll rotation equations are derived

to provide an example of the technique. The standard model structure for a least-squares regression:

$$z = X\theta + \varepsilon \tag{5.7}$$

Equation 5.7 can be rewritten in terms of a quadcopter dynamic model with angular acceleration being the dependent or response variable, and angular velocity and the roll input command being the regressor or explanatory variables. The unknown parameters to be estimated are the torque and damping constants. The roll input command ($Roll_{CMD}$) is multiplied by two when used in this study because it is being sent to each motor on the roll axis.

$$I_x\ddot{\theta} = -b_x\dot{\theta} + \Delta\tau + \varepsilon \tag{5.8}$$

The change in torque of the motor ($\Delta\tau$) can be rewritten in order to distinguish the regressor from the parameter.

$$\Delta\tau = LK_{FTR}(Roll_{CMD} * 2) \tag{5.9}$$

Substituting Equation 5.9 into Equation 5.8 yields:

$$\ddot{\theta} = \frac{-b_x\dot{\theta} + LK_{FTR}(Roll_{CMD} * 2) + \varepsilon}{I_x} \tag{5.10}$$

The resulting equation can then be expressed in linear regressor form where A,B, and C are the parameters estimated by the least squares estimation.

$$\ddot{\theta} = A\dot{\theta} + B(Roll_{CMD} * 2) + C \tag{5.11}$$

The recursive Fourier transform is applied to transform the data from the time domain to the desired frequency domain, w. The frequency domain w is comprised of a set of frequencies at which to compute the recursive Fourier transform. The frequency bin used herein was from 0.01Hz to 3Hz in steps of 0.04. The transform acts as a filter for the parameter estimation because motion outside the desired frequency range of the quadrotor has minimal influence on the vehicle dynamics. The Fourier transform is performed on the matrix of regressors by a forgetting factor, λ, which can vary between zero and one (Equation 5.12). A forgetting factor of $\lambda = 0$ conceptually states that no frequency data is retained from previous recursive Fourier transform calculations. Conversely, a forgetting factor of $\lambda = 1.0$ results in complete frequency information retainment. The corresponding parameter estimation is quite stable; however, the estimation can not adjust sufficiently for time-varying parameters. The forgetting factor used herein is $\lambda = 0.989$ and was empirically determined for the time varying nature of the parameters during induced failures.

$$X(w) = \sum_{i=0}^{N-1} x(i) e^{-jwi\Delta t} * \lambda \tag{5.12}$$

Once the data has been transformed into the frequency domain, the least squares equation error technique is used. Least squares can be done in the time domain or the frequency domain. Equation 5.12 is taking regressors in the time domain and putting them in the frequency domain to then perform the least squares. For more information on this method of parameter estimation, see "Real-Time Parameter Estimation in the Frequency domain" by Eugene Morelli [32]. The estimated parameters are determined by

minimizing the sum of the squared differences between the response variable and the linear regressor model. The estimation can be expressed as a function of all the parameters solved for (θ) in Equation 5.13.

$$J(\theta) = \frac{1}{2}\sum_{i=1}^{N}[z(i) - X^T(i) * \theta]^2 \tag{5.13}$$

Upon completing the Fourier transform regression (FTR), the parameter used to compare the two techniques is the motor torque constant, K_{FTR}.

$$K_{FTR} = \frac{BI_x}{L} \tag{5.14}$$

5.2.4 Testing Methodology

Testing was conducted first with the quadrotor constrained to only motion in the roll axis, then testing was conduced with the aircraft in free (unconstrained) flight. A static calibration of each quadcopter arm was performed in accordance with standard calibration procedures [1, 5] with two trials performed for each individual arm with ascending and descending applied loads. The calibration procedure performed provides estimates of the strain gauge-based estimation hysteresis, repeatability, and linearity. Each arm was calibrated to a rated capacity of 15.7N (3.5 lb.). [7]

The first phase of testing was in a benchtop environment. The quadcopter was suspended and fixed by two non-powered motors opposite each other, which allowed for the quadcopter to rotate in the roll axis seen in Figure 21.

The first phase of testing was focused on evaluating the detection capabilities of a

Figure 21: Single axis constrained full motor failure test setup

full motor failure in a safe way with minimal variables prior to unconstrained flight testing. In the testing scenario, the two free moving motors were given inputs for stabilized flight via the flight controller for a period of fifteen seconds while varying the roll angle for better parameter estimation. The roll angle was varied manually via remote control input by the operator. One motor was then completely failed for one second after which the stabilization flight controller recovered the aircraft to stabilized flight.

The second phase of testing was performed in an unconstrained flight test environment. Free-flight testing was performed in the UMKC Flight Testing Facility. The facility has a 6.1m x 6.1m x 3.1m (20ft x 20ft x 10ft) flight volume, and can be equipped with motion capture cameras (Figure 22). During each free-flight test, the quadrotor was flown at a steady state hover while periodically moving about the roll axis to excite the

roll command of the vehicle. While in a steady state hover, the user then manually input a partial motor failure (75% of the initial motor command) via remote control. The flight controller was unaware of the imposed failure.

Figure 22: UMKC Flight Testing Facility

Both phases of testing were performed in order to compare the two parameter estimation techniques. The purpose of the tests was to evaluate which parameter estimation technique could not only detect a failure faster, but which method also yields the most accurate results. The specific comparison made between the two parameter estimation methods is the motor torque constant. The motor torque constant is calculated using both the thrust estimation,K_{SG}, and real-time parameter estimation,K_{FTR}, techniques. The motor constant should converge to a constant value during steady state, and when a

failure or partial failure is implemented, the torque constant should decrease or increase depending on which motor the failure is implemented.

5.3 Results

5.3.1 Single Axis Constrained Full Motor Failure

The first flight test performed was a benchtop test in which the quadcopter was suspended and fixed by two non-powered motors. The results for the least squares parameter estimation and strain gauge estimated thrust force techniques for this test can be seen in Figure 23. There were multiple trials performed that depicted the same trend, however, one representation with both parameter estimation techniques used for analyzing the parameter estimation results. As mentioned previously, the parameter of interest is the motor torque constant. The graph on top shows the FTR technique, K_{FTR} vs time. The induced full motor failure is represented by the dotted line at about 12.5s. The graph in the middle is the strain gauge estimated thrust force technique, K_{SG} vs time. The graph below is Roll angle vs time, which is shown to give an intuitive representation of physical movement of the quadcopter when the motor fails. K_{SG} was calculated using Equation 5.6, and depicts asymptotic behavior. The asymptotic behavior comes from $Roll_{CMD}$ transitioning from positive to negative (or vise-versa)and causing a division by zero calculation. Table 6 shows the standard deviation from the mean of the motor torque constant for both parameter estimation techniques before and after the motor failure. As shown, the FTR method has a much smaller standard deviation overall, but takes longer to converge after the motor failure compared to the strain-gauge estimated thrust force

technique.

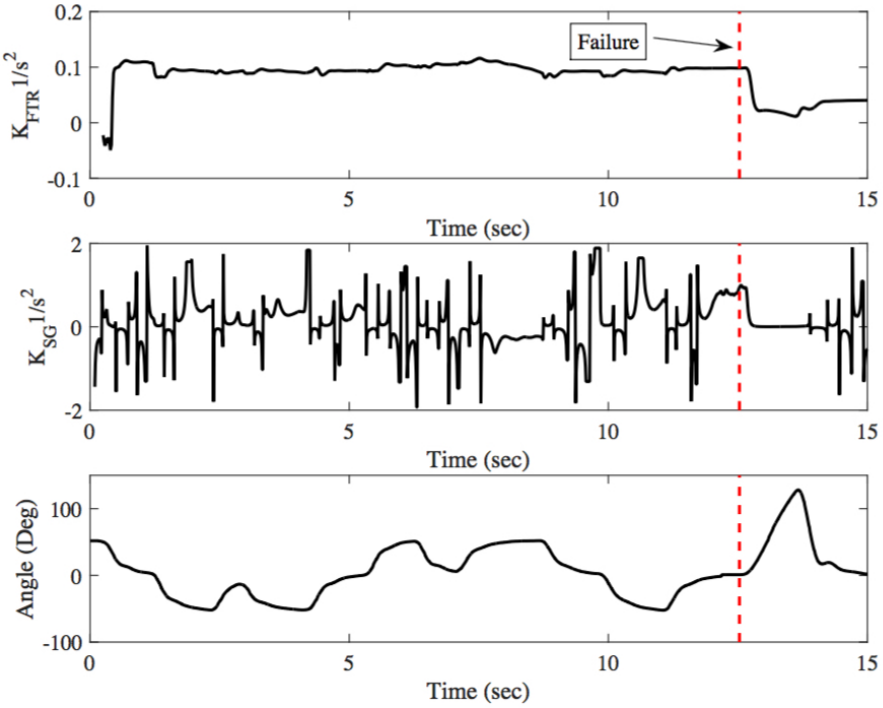

Figure 23: Single axis constrained full motor failure

Table 6: Standard deviations and convergence times for motor constants during full motor failure testing

	$\sigma_{BeforeFailure}$	$\sigma_{AfterFailure}$	TTC
K_{FTR}	$0.007\frac{1}{s^2}$	$0.022\frac{1}{s^2}$	0.38sec
K_{SG}	$0.591\frac{1}{s^2}$	$0.406\frac{1}{s^2}$	0.23sec

5.3.2 Free-Flight Partial Motor Failure

The results of the strain gauge estimated thrust force and FTR parameter estimation techniques for free-flight testing are shown in Figure 24. Roll maneuvers were

performed aggressively before a partial motor failure was manually induced, quickly leading the quadcopter to fall into a safety net in the UMKC flight-test facility. The user did however, attempt to recover from the failure by compensating with an increased roll command to the failed motor. The free flight tests were repeated in the same fashion several times and produced similar results. A representative trial of the flight testing results is shown in figure 24. The resultant figure is in the same format of figure 23 such that the graph on top is the FTR parameter estimation technique. The graph in the middle is the strain gauge estimated thrust force technique, and The graph below is the roll angle vs time to show intuitively what is happening to the quadcopter at the time of failure. The partial motor failure was implemented at 81.9sec and consequently induces a 30 degree roll angle deviation from the desired angle. Figure 24 shows only a small portion (7 seconds) of the entire flight test. This was done in order to more closely observe the failure event and the effect it has on a steady estimated motor constant.

As shown in Equation 4.2, translational motion data is required in addition to rotational motion data for the acceleration to be known at each motor location. For this study, the quadcopter rotation was of much more relevance, and the translational movement was considered to be negligible. In order to neglect this, motion capture data would be used, however for this study motion capture data was not readily available.

5.4 Discussion

The parameter estimation when using both the strain gauge force estimation and FTR techniques show a significant change in the motor torque constant of the quadcopter

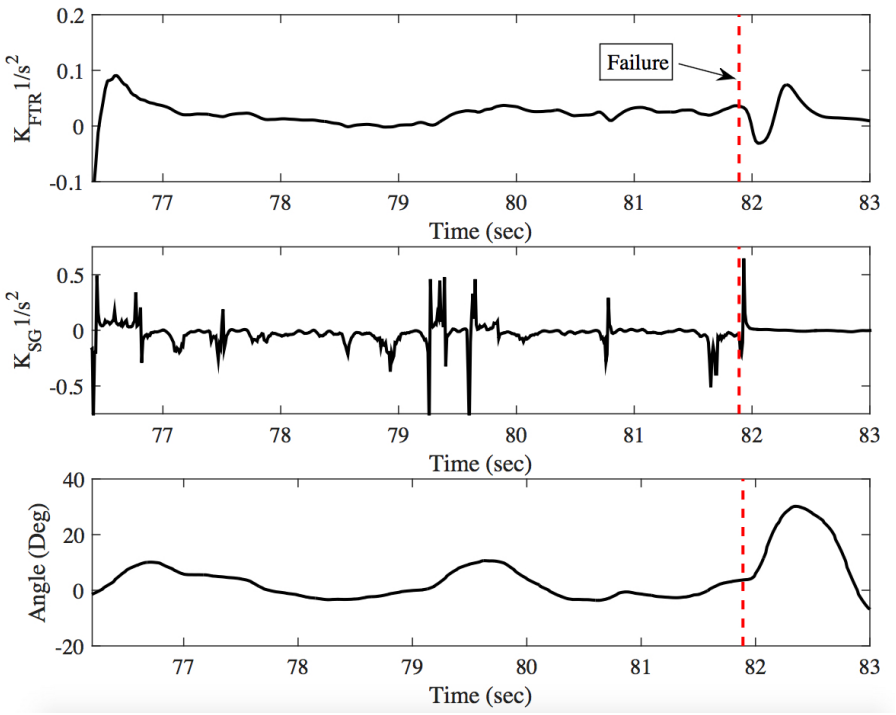

Figure 24: Torque constant parameter estimates during partial motor failure in unconstrained flight

when a motor failure is induced. For each parameter estimation technique, free-flight testing results show the motor torque constant converge and then diverge when the partial motor failure is induced on the aircraft. The strain gauge thrust estimation method does not show clear convergence before the induced motor failure during constrained testing. Shown in Tables 6 and 7, the standard deviation of the motor constant for the FTR technique is much smaller overall than the strain gauge estimated thrust force technique, but doesn't converge to a steady state value after failure as quickly as the strain gauge estimated thrust force technique. The strain gauge estimated thrust force technique has a large amount of noise in the parameter calculation. The noise in estimation could lead

Table 7: Standard deviations and convergence times of both technique motor constants for a partial motor failure

	$\sigma_{BeforeFailure}$	$\sigma_{AfterFailure}$	TTC
K_{FTR}	$0.034\frac{1}{s^2}$	$0.025\frac{1}{s^2}$	0.68sec
K_{SG}	$0.112\frac{1}{s^2}$	$0.072\frac{1}{s^2}$	0.11sec

to false detection; therefore, the point-to-point strain gauge-based estimation technique may not be the optimal choice for robust fault detection. One of the largest challenges in failure detection is finding a technique that is insensitive to noise, but can quickly detect a failure [32].

In the current forms, both techniques require persistent excitation in order to properly estimate the torque constant parameter. in this study, only the input roll command between the two motors normal to the axis in which the failure is occurring is known. The results are indicative that both methods could be used to detect a failure, but it is difficult to utilize the new torque constant to mitigate the failure as there is little physical meaning of the parameter. When all motors are functioning normally, the motor constant describes the conversion from input command to angular acceleration (Equation 5.11). If the input command is zero, then the angular acceleration is zero. If a motor fails (partial or full failure), an input command of zero will yield a nonzero angular acceleration. Therefore there is a new bias in the system that is not accounted for by the model. The value that the motor torque constant converges to before and after the failure in each test is inconclusive because the motors are coupled, and is representative of the motor couple or resultant torque.

The least squares parameter estimation yields potentially more accurate results than the strain gauge thrust estimation technique despite the inconclusive motor torque value convergence. This is possibly because the strain gauge thrust estimation is calculating the motor torque constant from point-to-point instead of doing the least squares fit of the data stored. As shown in Figure 23, there is noise as well as asymptotic behavior. An asymptote happens when $Roll_{CMD}$ cancels out between the two motors, which is inevitable when using a point-to-point method because stabilizing a quadcopter will result in a zero difference in $Roll_{CMD}$ as it shifts signs. A combination of strain gauge thrust estimation with a least squares fit technique may provide better results over either technique alone. A regressor model that implemented the measured or estimated thrust force from the strain gauges could be developed by identifying the estimated forces into the linear regressor equation. A potential combination of these two methods could effectively combine the smoothness of the least squares technique, while still maintaining a high level of sensitivity to failure detection from the strain gauge thrust estimation.

5.5 Conclusion and Future work

This chapter is an initial evaluation of two methods of parameter estimation. A previous study [7] showed feasibility of this strain gauge thrust estimation system for potential failure detection applications. Results indicated a high level of noise in the motor torque parameter estimate for the strain gauge-based technique, but the detection time was exceptionally quick. The objective of the work herein was to compare the feasible thrust estimation technique with a more traditional approach to parameter estimation specifically

during in-flight failures. A frequency domain least squares Fourier Transform Regression (FRT) was also tested in this study. The FTR method demonstrated feasibility in failure detection for a quadrotor, but requires individual motor persistent excitation which was not achieved in this study. A combination of the strain gauge thrust estimation system with the FTR method could potentially show success in parameter estimation and failure detection. The third objective of this thesis was to compare the strain gauge-based thrust estimation system to an indirect real time parameter estimation technique, which was not performed to completion with the conclusion above. Further investigation is required as to the quality of the strain gauge-based parameter estimation results to satisfy the third objective.

CHAPTER 6

CONCLUSION

The use of the strain gauge as a tool to aid in the development of two dynamic measurement systems has been shown. A circular parachute strain gauge-load distribution measurement system has been developed, tested, and validated in pursuit of completing the first thesis objective. The remaining thesis objectives were pursued with a strain gauge-based thrust estimation system for a quadrotor aerial vehicle being developed, tested, and compared against a more traditional real-time parameter estimation technique. The first two thesis objectives were met by developing and testing the proposed systems, but the third thesis objective was not completely met when comparing the two parameter estimation techniques. Further investigation is required as to the quality of the strain gauge-based parameter estimation technique's results.

To complete the first objective, a wireless load measurement system consisted of a redesigned signal conditioner and was coupled with a previously developed load cell design. The validated system developed has the potential to aid in the research and development of a wide range of aerodynamic descent vehicles. The small, non-invasive, and inexpensive system developed can be applied to ram-air parafoils and reversible reefing systems on circular parachutes. The load measurement system can aid in the design and further development of several aerodynamic decelerator systems.

An individual motor thrust estimation system for a quadcopter unmanned aerial

vehicle was developed and evaluated, completing the second objective. A custom strain gauge-embedded quadcopter frame was designed, calibrated, and evaluated via indoor free-flight testing with the use of a motion capture system. The strain gauge bending force reading was used to estimate the motor thrust force. Inertial forces caused by rotational and translational acceleration were compensated for using a dynamic model created using rigid body kinematics. The system demonstrated feasibility during high frequency motion, which warranted further investigation to its applicability for fault tolerance applications.

The third objective was pursued by performing an initial evaluation of two types of parameter estimation for the application of fault detection in a quadrotor UAV. The first technique evaluated was the strain gauge-based thrust estimation system described in the second objective. The second technique evaluated was a frequency domain least squares Fourier Transform Regression. The strain gauge-based thrust estimation system showed a high level of noise in the motor torque parameter estimate, but an exceptionally quick response to the quadrotor motor failure. The Fourier Transform Regression technique demonstrated feasibility in detecting a motor failure, but will require individual motor persistent excitation in order to properly estimate the motor torque constant.

The work presented in this thesis has aided in the advancement of strain gauge measurement technology. Strain gauges are used in the engineering community for a wide range of technical applications. The creation of new and innovative ways to implement strain gauges in mechanical systems will be pursued for ages due to their versatility, reliability, and cost effectiveness.

REFERENCE LIST

[1] United States Department of the Interior Bureau of Reclamation, "Procedure for Calibrating Force Transducers (Load Cells)," USBR 1045-89.

[2] A. Sanchez, L.R. Garcia Carrillo, E. R. R. L., and Garcia, O. Hovering Flight Imporvement of a Quad-rotor Mini UAV Using Brushless DC Motors. *Springer Science+Business Media B.V.* (September 1, 2010).

[3] Aguilar-Sierra, H., Flores, G., Salazar, S., and Lozano, R. Fault Estimation For a Quad-rotor MAV Using Polynomial Observer. *2013 Inernational Conference on Unmanned Aircraft Systems (ICUAS)* (May 2013, Atlanta, GA).

[4] Altug, E., Ostrowski, J. P., and Taylor, C. J. Quadrotor Control Using Dual Camera Visual Feedback. *IEEE International Conference on Robotics and Automation* (Taipei, Taiwan, September 2003).

[5] Anderson, G. B., and Raybold, R. C. Studies of Calibration Procedures for Load Cells and Proving Rings as Weighing Devices. *National Bureau of Standards*, NBSTN436 (1969).

[6] Basak, H., and Prempain, E. Switching Recovery Control of a Quadcopter UAV. *2015 European Control Conference (ECC), Year = July 17, 2015*.

[7] Bazin, J. M., Fields, T. D., and Smith, A. J. Feasibility of In-Flight Quadrotor Individual Motor Thrust Measurements. *2015 AIAA Science and Technology Forum and Exposition* (January 2015, San Diego, CA).

[8] Benney, R. History and Challenges of Airdrops in Afghanistan-Invited Lecture. *22nd AIAA Aerodynamic Decelerator Systems Conference and Seminar* (Daytona Beach, Florida, March 25-28, 2013).

[9] Bentley, P., Ed. *Evolutionary Design by Computers*. pp. 153-157, Morgan Kaufmann, San Francisco, 1999.

[10] Braun, R., and Manning, R. Mars exploration entry, descent and landing challenges. *2006 IEEE Aerospace Conference* (Big Sky, Montana, March 4-11, 2006).

[11] Butler, D. Dawn of the Age of the Drones: An Australian Privacy Law Perspective. *University of New South Wales Law Journal 37.2* (2014), 434–470.

[12] Cruz, J. R., Kandis, M., and Witkowski, A. Opening loads Analyses for Various Disk-Gap-Band Parachutes. *17th AIAA Aerodynamic Decelerator Systems Technology Conference and Seminar* (Monterey, CA, May 19-22, 2003).

[13] Desabrais, K. J., Lee, C. K., Buckley, J., and Jones, T. W. Experimental Parachute Validation Research Program and Status Report on Indoor Drop Tests. *19th AIAA Aerodynamic Decelerator Systems Technology Conference and Seminar* (Williamsburg, Virginia, May 21-24, 2007).

[14] DiCesare, A., Gustafson, K., and Lindenfelzer, P. Design Optimization of a Quad-Rotor Capable of Autonomus Flight. *Worchester Polytechnic Institute* (April, 2008).

[15] Dobrokhodov, V. N., Yakimenko, O. A., and Junge, C. J. Six-Degree-of-Freedom Model of a Controlled Circular Parachute. *Journal of Aircraft 40* (2003), 482–493.

[16] Ducard, G., and D'Andrea, R. Autonomous Quadrotor Flight Using a Vision System and Accomodating Frames Misaligment. *IEEE International Symposium on Industrial Embedded Systems* (Lausanne, July 2009).

[17] Fields, T. D. Development and Feasibility of a Non-Invasive Wireless Parachute Load Distribution Measuring System. *30th AIAA Aerodynamic Measurement Technology and Ground Testing Conference* (Atlanta, Georgia, June 16-20, 2014).

[18] Fields, T. D., Heninger, M. J., LaCombe, J. C., and Wang, E. L. In-flight Landing Location Predictions using Ascent Wind Data for High Altitude Balloons. *AIAA Balloon Systems Conference* (Daytona Beach, Florida, March 26-28, 2013).

[19] Fields, T. D., LaCombe, J. C., and Wang, E. L. Autonomous Guidance of a Circular Parachute Using Descent Rate Control. *Journal of Guidance, Control, and Dynamics 35*, 4 (2012), 1367–1370.

[20] Fields, T. D., LaCombe, J. C., and Wang, E. L. Flight Testing of a 1-DOF Variable Drag Autonomous Descent Vehicle. *22nd AIAA Aerodynamic Decelerator Systems Conference* (Daytona Beach, FL, March 25-28, 2013).

[21] Fields, T. D., LaCombe, J. C., and Wang, E. L. Path Planning for a Circular Parachute Using Descent Rate Control. *22nd AIAA Aerodynamic Decelerator Systems Conference* (Daytona Beach, FL, March 25-28, 2013).

[22] Freddi, A., Lanzon, A., and Longhi, S. A feedback linearization approach to fault tolerance in quadrotor vehicles. *Proceedings of the 2011 IFAC World Congress* (Milan, Italy, 2011).

[23] Goodrich, M. A., Morse, B. S., Gerhardt, D., Cooper, J. L., Quigley, M., Adams, J. A., and Humphrey, C. Supporting Wilderness Search and Rescue using a Camera-Equipped Mini UAV. *Journal of Field Robotics 25*, 1-2 (2007), 89–110.

[24] Hanssen, S. Drone class: Keeping coursework current as technology advances. *Community College Journal of Research and Practice* (2016), 1–4.

[25] Hoffmann, G. M., Huang, H., Waslander, S. L., and Tomlin, C. J. Quadrotor helicopter flight dynamics and control: Theory and experiment. *AIAA Guidance, Navigation, and Control Conference* (Hilton Head, South Carolina, August 20-23, 2007).

[26] Hoffmann, G. M., Huang, H., Waslander, S. L., and Tomlin, C. J. Precision flight control for a multi-vehicle quadrotor helicopter testbed. *Control Engineering Practice* (June 23, 2011).

[27] Knacke, T. Parachute Recovery Systems. *Para-Publishing* (Santa Barbara, California, 1992).

[28] Lange, S., and Protzel, P. Cost-Effective Mono-Camera Tracking System for a Multirotor UAV Aimed for Hardware-in-the-Loop Experiments, 2012.

[29] Lee, C. K. Experimental Investigation of Full-Scale and Model Parachute Opening. *8th AIAA Aerodynamic Decelerator and Balloon Technology Conference* (Hyannis, Massachusetts, April 2-4, 1984).

[30] Leers, J. Een Parachute. *De prins der gillustreerde bladen* (February 18, 1911).

[31] Mitiguy, P. *Advanced Dynamics and Motion Simulation*. Prodigy Press, 2014.

[32] Morelli, E. A. Real-Time Parameter Estimation in the Frequency Domain. *Journal of Guidance, Control, and Dynamics 39* (September 2000).

[33] Morris, A. Summary of Generation II CPAS Parachute Performance. *21st AIAA Aerodynamics Decelerator Systems Technology Conference* (Dublin, Ireland, May 2011).

[34] Morris, A. L., Taylor, T., and Olson, L. Load Asymmetry Observed During Orion Main Parachute Inflation. *21st AIAA Aerodynamic Decelerator Systems Conference and Seminar* (Dublin, Ireland, May 23-26, 2011).

[35] NI-Tutorial-3642. Measuring Strian with Strain Gauges.

[36] Poole, L. R. Force-Strain Characterisitcs of Dacron Parachute Suspension-Line Cord Under Dynamic Loading Conditions. *4th AIAA Aerodynamic Decelerator Systems Conference* (May 1973, Palm Springs, Florida).

[37] Quigley, M., Goodrich, M. A., Griffiths, S., Eldredge, A., and Beard, R. W. Target Acquisition, Localization, and Surveillance Using a Fixed-Wing Mini-UAV and Gimbaled Camera. *Proceedings of the 2005 IEEE International Conference on Robotics and Automation* (Barcelona, Spain, April 2005).

[38] Quilter, M. C. Vegetation monitoring using low-altitude, large-scale imagery from radio-controlled drones. *Thesis (Ph.D.) Brigham Young University* (1997).

[39] Remondino, F., Barazzetti, L., Nex, F., Scaioni, M., and Sarazzi, D. UAV Photogrammetry for Mapping and 3D Modeling - Current Status and Future Perspectives. *International Archives of the Photogrammetry, Remote Sensing, and Spatial Information Sciences XXXVIII-1/C22* (2011).

[40] Schmidt, J. Ares 1 Main Parachute Cluster Asymetrical Loading and Design Recommendations. *United Space Alliance* (January 7, 2010).

[41] Sharifi, F., Mirzaei, M., Gordon, B. W., and Zhang, Y. Fault Tolerant Control of a Quadcopter UAV using Sliding Mode Control. *2010 Conference on Control and Fault Tolerant Systems* (Nice, France, October 6-8, 2010).

[42] Siefers, T., Greene, K., McLaughlin, T. E., and Bergeron, K. Wind and Water Tunnel Measurements of Parachute Suspension Line. *51st AIAA Aerospace Sciences Meeting* (January 2013, Dallas, Texas).

[43] Slegers, N. Effects of Canopy-Payload Relative Motion on Control of Autonomous Parafoils. *Journal of Guidance, Control, and Dynamics 33*, 1 (2010), 116–125.

[44] Slegers, N., Beyer, E., and Costello, M. Use of Variable Incidence Angle for Glide Slope Control of Autonomous Parafoils. *Journal of Guidance, Control and Dynamics 31*, 3 (2008), 585–596.

[45] Smith, A. J., Fields, T. D., Wang, E. L., and LaCombe, J. C. Low Cost Alternative to Motion Capture Systems for Indoor Flight Testing Using On-board Computer Vision. *AIAA Atmospheric Flight Mechanics Conference* (San Diego, California, 2016).

[46] S.O. Link, M. T., and van Bravel, M.

[47] Stein, P. K. Strain Gauge History and the End of the Twentieth Century. *Experimental Techniques* (March 2001).

[48] Taillier, S. Drone operator fined after UAV crashed into Geraldton trialthlete. *Australian Broadcasting Corporation* (November 12, 2014).

[49] Talanova, J. Drone slams into seating area at U.S. Open; teacher arrested. *CNN News* (September 5, 2015).

[50] Uchiyama, M., and Kitagaki, K. Dynamic Force Sensing for High-Speed Robot Manipulation Using Kalman Filtering Techniques. *28th Conference on Decision and Control* (Tampa, Florida, 1989).

[51] W. Gray, J. Palmer, J. G. M. G., and Iannotti, F.

[52] Ward, M., and Costello, M. Autonomous Control of Parafoils Using Upper Surface Spoilers. *22nd AIAA Aerodynamic Decelerator Systems Conference and Seminar* (Daytona Beach, Florida, March 25-28, 2013).

[53] White, L. The Invention of the Parachute. *Technology and Culture* (July 1968).

[54] Whitlock, C. When Drones Fall From the Sky. *The Washington Post* (June 20, 2014).

[55] Yakimenko, O. On the Development of a Scalable 8-DoF Model for a Generic Parafoil-Payload Delivery System. *18th AIAA Aerodynamic Decelerator Systems Technology Conference and Seminar* (May 23-26, 2005, Munich, Germany).

[56] Younes, Y. A., Noura, H., Rabhi, A., Hajjaji, A. E., and Hussien, N. A. Sensor Fault Detection and Isolation in the Quadrotor Vehicle Using Nonlinear Identity Observer Approach. *2013 Conference on Control and Fault-Tolerant Systems (SysTol* (October 2013, Nice, France).

[57] Young, W. R. The Helicopters (Epic of Flight).

VITA

John Bazin was born on August 10, 1991 in New York, New York. He went to public school until attending Rockhurst Highschool in Kansas City, Missouri, and graduated in 2010. He then attended and graduated from the University of Missouri-Kansas City with a Bachelor of science in Mechanical engineering in August, 2015. He did this while also starting his master's degree program at the University of Missouri-Kansas City at the same time in their BS/MS five year program.